



HAL
open science

The role of the intra-daily SST variability in the Indian monsoon variability and monsoon-ENSO–IOD relationships in a global coupled model

Pascal Terray, Kakitha Kamala, Sébastien Masson, Gervan Madec, A. K. Sahai, Jing-Jia Luo, Toshio Yamagata

► To cite this version:

Pascal Terray, Kakitha Kamala, Sébastien Masson, Gervan Madec, A. K. Sahai, et al.. The role of the intra-daily SST variability in the Indian monsoon variability and monsoon-ENSO–IOD relationships in a global coupled model. *Climate Dynamics*, 2012, 39, pp.729-754. 10.1007/s00382-011-1240-9 . hal-01322976

HAL Id: hal-01322976

<https://hal.science/hal-01322976>

Submitted on 29 May 2016

HAL is a multi-disciplinary open access archive for the deposit and dissemination of scientific research documents, whether they are published or not. The documents may come from teaching and research institutions in France or abroad, or from public or private research centers.

L'archive ouverte pluridisciplinaire **HAL**, est destinée au dépôt et à la diffusion de documents scientifiques de niveau recherche, publiés ou non, émanant des établissements d'enseignement et de recherche français ou étrangers, des laboratoires publics ou privés.

1 The role of the intra-daily SST variability
2 in the Indian Monsoon variability and monsoon-ENSO-IOD relationships
3 in a global coupled model

4

5

6 Pascal Terray¹, Kakitha Kamala¹, Sébastien Masson¹, Gervan Madec¹,

7 A. K. Sahai², J.-J. Luo³ and Toshio Yamagata³

8

9

¹LOCEAN/IPSL, CNRS/IRD/UPMC/MNHN, Paris, France

10

²Indian Institute of Tropical Meteorology, Pune, India

11

³RIGC, Yokohama, Japan

12

13

14

15

16

17

18

19

Revised for *Climate Dynamics*

20

21

October 2011

Corresponding author address: Pascal Terray, LOCEAN-IPSL, Université Pierre et Marie Curie, BP100 – 4 place Jussieu, 75252 Paris cedex 05, France.

Tel : +33 1 44 27 70 78

E-mail : terray@locean-ipsl.upmc.fr

ABSTRACT

22
23
24
25
26
27
28
29
30
31
32
33
34
35
36
37
38
39
40
41
42
43
44
45
46
47
48
49
50
51
52
53
54
55
56

The impact of diurnal SST coupling and vertical oceanic resolution on the simulation of the Indian Summer Monsoon (ISM) and its relationships with El Niño-Southern Oscillation (ENSO) and Indian Ocean Dipole (IOD) events are studied through the analysis of four integrations of a high resolution Coupled General Circulation Model (CGCM), but with different configurations. The only differences between the four integrations are the frequency of coupling between the ocean and atmosphere for the Sea Surface Temperature (SST) parameter (2 vs 24 hours coupling) and/or the vertical oceanic resolution (31 vs 301 levels) in the CGCM.

Although the summer mean tropical climate is reasonably well captured with all the configurations of the CGCM and is not significantly modified by changing the frequency of SST coupling from once to twelve per day, the ISM-ENSO teleconnections are rather poorly simulated in the two simulations in which SST is exchanged only once per day, independently of the vertical oceanic resolution used in the CGCM.

Surprisingly, when 2 hours SST coupling is implemented in the CGCM, the ISM-ENSO teleconnection is better simulated, particularly, the complex lead-lag relationships between the two phenomena, in which a weak ISM occurs during the developing phase of an El Niño event in the Pacific, are closely resembling the observed ones. Evidence is presented to show that these improvements are related to changes in the characteristics of the model's El Niño which has a more realistic evolution in its developing and decaying phases, a stronger amplitude and a shift to lower frequencies when a 2-hourly SST coupling strategy is implemented *without any significant changes in the basic state of the CGCM*. As a consequence of these improvements in ENSO variability, the lead relationships between Indo-Pacific SSTs and ISM rainfall resemble the observed patterns more closely, the ISM-ENSO teleconnection is strengthened during boreal summer and ISM rainfall power spectrum is in better agreement with observations. On the other hand, the ISM-IOD teleconnection is sensitive to both SST coupling frequency and the vertical oceanic resolution, but increasing the vertical oceanic resolution is degrading the ISM-IOD teleconnection in the CGCM.

These results highlight the need of a proper assessment of both temporal scale interactions and coupling strategies in order to improve current CGCMs. These results, which must be confirmed with other CGCMs, have also important implications for dynamical seasonal prediction systems or climate change projections of the monsoon.

Keywords: Indian summer monsoon; El Niño-Southern Oscillation; long-range predictability; ocean-atmosphere interactions; coupled climate model.

57 **1. Introduction**

58

59 During the months of June through September, the rainfall associated with the Indian
60 Summer Monsoon (ISM) provides the main source of fresh water for millions of people over
61 the Indian subcontinent. Predicting ISM onset and amplitude, both on the seasonal and
62 interannual time scales, is thus not only a challenging scientific issue, but also a key societal
63 need for South Asian countries. As such, the relative role of remote and local Sea Surface
64 Temperature (SST) forcing in shaping ISM rainfall anomalies was investigated by many
65 observational and modeling studies (see Webster et al., 1998; Wang, 2006 for reviews). One
66 main conclusion from these previous works is that a primary key to cause ISM variability at
67 the interannual time scale arise from teleconnection with the tropical Pacific Ocean and is
68 related to the El-Niño Southern Oscillation (ENSO) phenomenon in the Pacific. While ENSO
69 is still regarded as one of the main factors of ISM variability, the ISM-ENSO relationship has
70 weakened during recent decades or more exactly has changed in nature for reasons which are
71 still a matter of debate (Krishna Kumar et al., 1999, 2006; Gershunov et al., 2001; Ashok et
72 al., 2001, 2004; Kinter et al., 2002; Annamalai et al., 2007; Kucharski et al., 2007, 2008;
73 Xavier et al., 2007; Boschat et al., 2011a, 2011b).

74 Connections between tropical Indian Ocean variability, especially its dominant mode of
75 variability, the Indian Ocean Dipole (IOD), tropical Atlantic and ISM have also been noticed
76 by many recent studies (Meehl and Arblaster, 2002; Loschnigg et al., 2003, Li et al., 2006;
77 Meehl et al., 2003; Ashok et al., 2001, 2004; Gadgil et al., 2005; Kucharski et al., 2007, 2008;
78 Krishnan and Swapna, 2009). Several authors (Ashok et al., 2001, 2004; Abram et al., 2008)
79 have suggested that the frequent occurrence of IOD events is the cause for the recent
80 weakening of the ISM-ENSO relationship. However, a general consensus on the influence
81 exerted by IOD or Atlantic Ocean on ISM rainfall variability has not been established so far
82 from the observations or atmospheric forced simulations. Because of the dynamically
83 interactive nature of the tropical ocean-atmosphere system and the near-global patterns of the
84 teleconnections associated with the Asian monsoon, global Coupled General Circulation
85 Models (CGCM) are instrumental in clarifying the basic mechanisms and feedbacks involved
86 in ISM variability and ISM-ENSO-IOD interactions (Lau and Nath, 2004; Fischer et al.,
87 2005; Behera et al., 2006; Wu and Kirtman, 2003, 2005, 2007; Terray et al., 2007; Bracco et
88 al., 2007; Krishnan et al., 2010). Thus, improving our understanding of ISM variability will
89 require the use of state-of-the-art CGCMs that attempt to represent all the processes that may

90 be important and that realistically simulate IOD, ISM and ENSO phenomena, a challenging
91 task for current CGCMs (Spencer et al., 2005; Joseph and Nigam, 2006; Annamalai et al.,
92 2007; Bracco et al., 2007; Cai et al., 2009). Based on all these concerns, we need to develop
93 accurate global CGCMs to gain more insight into the dynamics and predictability of ISM at
94 both the intraseasonal, interannual and decadal time scales (Wang et al., 2005; Krishna Kumar
95 et al., 2005; Wu et al., 2006; Wu and Kirtman, 2007).

96 However, the inherent limitations and flaws of current state-of-the-art CGCMs mean that
97 they cannot be exclusively relied upon for seasonal forecasting or climate change sensitivity
98 studies (Turner et al., 2005; Annamalai et al., 2007; Manganello and Huang, 2009; Cai et al.,
99 2009). As an illustration, skill scores of dynamical seasonal prediction systems for ISM
100 rainfall are very limited and still inferior to simple statistical models, even in the European
101 DEMETER project where multi-model ensemble was created from seven different CCGMs
102 (Palmer et al., 2004). In particular, recovering the complex ISM-ENSO teleconnections,
103 which is of paramount importance for the seasonal forecasting of ISM rainfall, remains a very
104 difficult task for recent CGCMs, as exemplified by Figure 1, which shows the lead-lag
105 relationships between ISM rainfall and Niño-3.4 SSTs in observations and as simulated by
106 several CCGMs participating in the third Coupled Model Intercomparison Project (CMIP3;
107 Meehl et al., 2007). Most of the CMIP3 CGCMs are able to recover the negative correlation
108 between the two phenomena during the monsoon season (from June to September), but the
109 most striking feature is that almost all of the CMIP3 coupled models fail to recover the
110 observed lead-lag relationships between Niño-3.4 SSTs and ISM, including the spring
111 predictability barrier, which is manifested as the transition from positive to negative
112 correlations prior to the ISM onset (Webster et al., 1998). Starting six months before ISM, the
113 correlation between Niño-3.4 SSTs and ISM rainfall is already negative in nearly all CGCMs
114 (Fig. 1). The amplitude of this negative correlation increases until the early ISM (June and
115 July) and fades away very rapidly during the late ISM and the following months in the
116 coupled simulations contrary to that observed. The physical factors, which are responsible of
117 this failure of most current CGCMs, must be investigated carefully if we want to improve the
118 skill of seasonal dynamical predictions or climate change projections for the ISM (Gadgil et
119 al., 2005). Furthermore, the realistic simulation of the relationships between ISM, ENSO and
120 IOD, which are indeed responsible for the main modes of interannual variability over India
121 and the tropical Indian Ocean, represents a unique benchmark for evaluating current state-of-
122 the-art CGCMs (Saji et al., 2006; Joseph and Nigam, 2006; Annamalai et al., 2007; Cai et al.,
123 2009).

124 The purpose of this paper is to investigate how accurately the relationships between ISM,
125 ENSO and IOD can be simulated by different configurations of the same CGCM with a
126 special focus on the impact of upper oceanic structures with small vertical and temporal scales
127 that can influence the development of large scale coupled phenomena such as ISM, IOD and
128 ENSO through scale interactions and ocean-atmosphere coupling (Meehl et al., 2001). To do
129 so, we analyze model outputs from four long integrations of the same CGCM, but with
130 different configurations differing only by the frequency of SST coupling and the vertical
131 oceanic resolution in the CGCM. A companion paper is specifically assessing how ENSO
132 structure, periodicity and feedbacks are modified in the different configurations of the same
133 CGCM (Masson et al., 2011).

134 The paper is organized as follows: in Section 2, we will describe the CGCM, the
135 experimental design for the different configurations of the CGCM, the datasets and the
136 statistical tools used. Section 3 will look at the mean boreal summer climate as simulated by
137 the different configurations of the CGCM, noting any significant differences between them.
138 The changes in ENSO and IOD variability are documented in Section 4. The ISM interannual
139 variability and the ISM-ENSO-IOD relationships as simulated in the different experiments are
140 analyzed in Section 5. Conclusions follow in Section 6.

141

142 **2. Model, experimental set up, datasets and statistical tools**

143

144 (a) *The SINTEX-F2 high-resolution coupled model*

145

146 The CGCM used in this study belongs to the family of SINTEX models (Guilyardi et al.,
147 2003; Gualdi et al., 2003; Luo et al., 2003). It is an upgraded version of SINTEX-F1 CGCM
148 (Luo et al., 2003; Luo et al. 2005). A new version has been developed (SINTEX-F2
149 hereafter). Its oceanic component is NEMO (<http://www.nemo-ocean.eu>; Madec, 2008;
150 Madec et al., 1998) including LIM2 (Timmermann et al., 2005) for the sea-ice model. We use
151 the configuration known as “ORCA05” which is a tri-polar global grid with a resolution of
152 0.5° by $0.5^\circ \cos(\text{latitude})$. Vertical resolution (31 or 301 levels depending on the
153 configurations, see below) and mixing are similar to Molines et al. (2006). The atmospheric
154 component consists of ECHAM5.3 (Roeckner et al., 2003, 2004) with a T106 horizontal
155 resolution and 31 hybrid sigma-pressure levels. A mass flux scheme (Tiedtke, 1989) is
156 applied for cumulus convection with modifications for penetrative convection according to
157 Nordeng (1994). The coupling information, without any flux correction, is exchanged every

158 two hours (24 hours for the SST parameter in the 24h31 and 24h301 configurations described
159 below) by means of the OASIS 3 coupler (Valcke, 2006). See Masson et al. (2011) for more
160 details.

161

162 (b) *Experimental set up*

163

164 Several previous studies have highlighted the potential role of the diurnal cycle on the
165 mean state, intraseasonal and interannual variabilities of the Indo-Pacific climate through
166 nonlinear scale interactions (Slingo et al., 2003; Danabasoglu et al., 2006; Bernie et al., 2007,
167 2008; Kawai and Wada, 2007; Ham et al., 2010). Motivated by these evidences, four long
168 integrations of the updated SINTEX-F2 CGCM have been realized using different modeling
169 strategies with a special focus on the impact of diurnal SST coupling and vertical oceanic
170 resolution on ENSO, IOD and ISM. Table 1 summarizes the numerical experiments
171 performed and their main characteristics. As seen in Table 1, all the configurations share the
172 same atmospheric component at T106L31 resolution and differ only by the SST coupling
173 frequency (2 hours vs 24 hours) and/or the vertical oceanic resolution in the high-resolution
174 CGCM (31 vs 301 levels). Thus, it is important to keep in mind that the coupling frequency
175 for all other parameters than the SST remains to be 2 hours (see Table 1). No flux correction
176 was applied, and the CGCM does not exhibit significant climate drift in the four long-term
177 simulations used here (not shown). In all the following analyses, the first 10 years of the
178 simulations have been excluded in order to minimize the biases due to the spin-up of the
179 CGCM.

180 The pathways by which the diurnal cycle may impact longer time scales may be classified
181 in two categories (i) the atmospheric contribution represented by the role of the solar cycle in
182 the air-sea coupling (Danabasoglu et al., 2006; Ham et al., 2010), and (ii) the oceanic
183 contribution, which corresponds to the response of the coupled system to the SST diurnal
184 cycle and high frequency variability (Slingo et al., 2003; Bernie et al., 2007, 2008). Our main
185 focus here is to detail the response of the interannual variability of the coupled system to the
186 SST diurnal and high frequency variability (e.g. oceanic contribution) since this question has
187 not been investigated in the previous studies (Slingo et al., 2003; Bernie et al., 2007, 2008).
188 Hence, the four experiments summarized in Table 1 were specifically designed to
189 discriminate the impact of the SST diurnal and high frequency variability from the solar cycle
190 response of the climate system. In this respect, it is worth noting that the experimental set up
191 used here is slightly different from those reported in Danabasoglu et al. (2006) or Ham et al.

192 (2010) in which twin coupled experiments using 1-day vs diurnal air–sea coupling frequency
193 for all the parameters (and not only the SST) are compared. With diurnal coupling frequency
194 for all the air-sea fluxes it is not possible to differentiate the relative role of the SST high
195 frequency variability from the solar cycle response.

196

197 (c) *Datasets and statistical tools*

198

199 Various datasets have been used to evaluate the model’s performance and to provide a
200 comprehensive description of ISM variability and its links with ENSO and IOD in the
201 different configurations.

202 Monthly-mean winds are from the National Centers for Environmental Prediction/National
203 Center for Atmospheric Research reanalysis (NCEP/NCAR, Kalnay et al. 1996). The period
204 from 1979 to 2008 has been used to compute the wind climatology. Since precipitation is
205 regarded as one of the least reliable fields from reanalyses, we use the 1979–2008 monthly
206 mean data from the Climate Prediction Center (CPC) Merged Analysis of Precipitation for the
207 observed rainfall (CMAP, Xie and Arkin 1997). However, to study ISM variability and its
208 teleconnections with ENSO and IOD on longer periods comparable to the length of the four
209 integrations of the coupled model, the classical All-India-Rainfall (AIR) dataset, based on
210 rain-gauge data, has also been considered (Parthasarathy et al., 1994). The SST dataset
211 selected for the study is the Hadley Centre Sea Ice and sea surface temperature dataset
212 (HadISST1.1) developed by Rayner et al. (2003). The surface heat fluxes analyzed here are
213 derived from products of the objectively analyzed air-sea fluxes (OAFlux) for the Global
214 Oceans project (Yu et al., 2008) and are obtained from the Woods Hole Oceanographic
215 Institute through <ftp://ftp.whoi.edu/pub/science/oaflux/data>. Finally, the Simple Ocean Data
216 Assimilation (SODA) version 2.0.2 (Carton et al. 2005) is used for diagnosing the
217 thermocline depth in the eastern Indian Ocean in Section 3. SODA 2.0.2 covers the period
218 from 1958 to 2001.

219 The statistical tools used here include mainly spectral analysis based on a Fast Fourier
220 Transform algorithm (Welsch, 1967) and a large battery of statistical tests to detect statistical
221 significant differences in power density between two frequencies or two ranges of frequencies
222 in different power spectra. For the sake of brevity, details about these statistical tests are not
223 given here and the interested reader is referred to Masson et al. (2011). Standard correlation
224 analysis has also been used to assess the ISM-ENSO-IOD relationships and the space-time
225 evolution of Indo-Pacific SSTs associated with ENSO in Section 5. The statistical

226 significance levels for the correlation coefficients have been estimated using the phase-
227 scrambling bootstrap test proposed by Ebisuzaki (1997) with 999 samples. This statistical test
228 takes directly into account the autocorrelation characteristics of the time series for assessing
229 the confidence level of the correlations.

230

231 **3. The coupled GCM boreal summer mean climate**

232

233 The overall performance of SINTEX-F2 has already been examined in Masson et al.
234 (2011) and is thus not repeated here. Instead, we will mainly focus in this section on salient
235 features of the simulated tropical climate that will be relevant to interpret the results reported
236 in the next sections and, more particularly, on the significant differences, if any, between the
237 basic state of the monsoon and the tropical Indian Ocean in the different configurations.

238

239 (a) *Boreal summer mean state*

240

241 The observed boreal summer (i.e., during June to September - JJAS) mean climatologies
242 and differences with the four configurations for SST, precipitation and 850 hPa wind are
243 shown in Figures 2, 3 and 4, respectively.

244 SST biases have a longitudinal distribution with a warm bias in the tropics and a cold bias
245 at mid-latitudes (Fig. 2). Note that contrary to many coupled models (Reichler and Kim,
246 2008), SINTEX-F2 does show only a weak “cold tongue” bias in the equatorial Pacific,
247 especially if the vertical oceanic resolution is increased (see Figs. 2d, e). However, the
248 tropical warm bias remains too strong and is more pronounced to the north of the equator and
249 in the upwelling regions of the three oceanic basins during boreal summer. Poor
250 representation of coastal regions and upwelling processes in coarse ocean model and a lack of
251 proper simulation of air-sea interactions are plausible causes for these large SST biases in the
252 western Indian, eastern Pacific and Atlantic oceans. Note, however, that increasing the
253 vertical oceanic resolution (e.g. the 2h301 and 24h301) does not reduce the warm bias in the
254 upwelling regions (see Figs. 2d, e).

255 Over the Indian Ocean, the CGCM shows an overall overestimation of the SST
256 climatology in the western Indian Ocean, excepted in a narrow band along the Somali and
257 Arabian coasts which is affected by a cold bias of $-1/2^{\circ}\text{C}$ in the four simulations. The warm

258 (cold) bias of the western (eastern) Indian Ocean leads also to an erroneous weak or even
259 reversed equatorial SST gradient over the Indian Ocean (see Fig. 5). Furthermore, this bias is
260 slightly enhanced with increased oceanic resolution.

261 The coupled simulation of Indo-Pacific rainfall climatology has been proven to be a rather
262 difficult test for current CGCMs (Wang, 2006). However, in all the configurations, SINTEX-
263 F2 reproduces a reasonable precipitation pattern during boreal summer (Fig. 3). As an
264 illustration, the CGCM simulates the maximum rainfall with more intensity to the north of the
265 equator and the large-scale spatial features associated with the Inter Tropical Convergence
266 Zone (ITCZ) band across the tropical Pacific, Indian and Atlantic oceans. For comparison, we
267 have also computed the differences between CMAP and Global Precipitation Climatology
268 Project (GPCP) analyses for the same base period (Fig. 3d). The rainfall amounts over the
269 ocean are systematically lower (about 15% lower) in the GPCP dataset (as already discussed
270 in Annamalai et al. (2007), these differences may be due to the fact that the GPCP data were
271 not tied as closely to atoll gauge estimates as CMAP data). Interestingly, in many regions, the
272 model's biases are of the same order of magnitude than the differences between GPCP and
273 CMAP datasets. However, as seen in Figure 3, there exists a tendency to a slight northward
274 shift of the ITCZ in all versions of the CGCM during boreal summer, even though this
275 systematic error is largely reduced if the GPCP dataset is used in the comparison (not shown).
276 In the western Pacific, 2h301 and 24h301 develop less precipitation than 2h31 and 24h31,
277 respectively, a feature consistent with the reduced "cold tongue" bias and zonal SST gradient
278 across the Pacific in the 2h301 and 24h301 configurations (Figs. 2 and 3).

279 Focusing now more specifically on the regional features associated with the ISM, we
280 observe that the CGCM fails to simulate the heavy rainfall band over the south equatorial
281 Indian Ocean, which is one of the important heat source for ISM rainfall variability
282 (Annamalai and Liu, 2005; Annamalai and Sperber, 2005; Goswami et al., 2006; Terray et al.,
283 2007). Furthermore, all the configurations overestimate precipitation over the Indian Ocean,
284 north of the equator, while the Indian subcontinent is dryer than observed. These enhanced
285 rainfall in the western and central equatorial Indian Ocean and deficient rainfall over the
286 Western Ghats are well-known biases of the ECHAM atmospheric model (Roeckner et al.,
287 1996) and are also found in previous versions of the SINTEX model (Terray et al., 2005b;
288 Cherchi et al., 2007). A possible explanation for this incorrect location of the ITCZ is that
289 SINTEX does not reproduce the correct pole-to-equator gradient in the Indian sector.
290 Unrealistic heavy rainfall over the northeastern part of the Indian subcontinent and the
291 Tibetan plateau is also seen in all configurations. This last problem may be related to model

292 precipitation parameterization or the representation of the orography and is also a common
293 bias of many current CGCMs (see Fig. 1 of Annamalai et al., 2007).

294 Over the tropical Indo-Pacific regions, the main features of the 850 hPa wind are
295 reasonably well captured by SINTEX-F2 (Fig. 4). Consistent with the reduced “cold tongue”
296 bias, the easterly trade winds are not too strong over the equatorial central Pacific. The
297 SINTEX-F2 model is also able to capture the major features of monsoon circulation, such as
298 the strong low-level jet from the Arabian Sea into South Asia and the southeasterly trade
299 winds in the south tropical Indian Ocean. The differences between NCEP and SINTEX-F2
300 850 hPa wind climatologies clearly show that the most important and robust systematic error
301 in the Indian region is the existence of an anomalous cyclonic cell over the equatorial western
302 and central Indian Ocean (Fig. 4). This cyclonic low-level circulation is consistent with the
303 rainfall biases discussed above. In all the configurations, the cross-equatorial component of
304 the flow extends too far eastward rather than being confined along the African coast.
305 Moreover, these strong winds increase evaporation over the eastern Indian Ocean, which in
306 turn may help maintain the erroneous SST gradient between the South-East Indian Ocean
307 (SEIO) and the western Indian Ocean (see Fig. 5f).

308 However, a known systematic error of the SINTEX model, which is probably the main
309 factor responsible for the SST biases in the eastern Indian Ocean, is the tendency to have a
310 shallow (deeper) thermocline in the eastern Indian Ocean during boreal summer and fall
311 (winter and spring). The thermocline-surface coupling is thus amplified in the annual cycle
312 with deeper and cooler water easily upwelled at the surface during boreal summer and fall,
313 cooling drastically the SEIO SSTs (Figs. 2 and 5; see also Fischer et al., 2005). In other
314 words, it is clear that the low-level wind, SST and precipitation errors in the eastern equatorial
315 Indian Ocean are intimately linked together. A warm bias, which is constant throughout the
316 annual cycle, is also found in the western Indian Ocean (Fig. 5a). This warm bias seems to be
317 the main factor responsible for the erroneous SST gradient over the equatorial Indian Ocean
318 during boreal summer (see Fig. 2). All these coupled errors are also seen when the vertical
319 oceanic resolution is increased (e.g. 2h301 and 24h301).

320

321 (b) *Climatological seasonal cycle in the Indian areas*

322

323 The ISM and IOD are both strongly phase-locked to the annual cycle, so to simulate both
324 phenomena accurately the CGCM must recover certain aspects of the seasonal cycle.

325

326 To look at the timing and extent of the monsoon in each of the configurations, Figure 6
327 shows the annual cycle of simulated and observed ISM rainfall indices. The ISM rainfall
328 indices are defined as the area-averaged precipitation over all land grid-points in the domain
329 65° - 95° E, 8° - 35° N (CMAP is used for the observations). The model simulates a reasonable
330 rainfall annual cycle in the Indian areas with a summer precipitation maximum as in observed
331 climate. All the configurations underestimate the rainfall intensity during the monsoon season
332 consistent with the results of Figs. 3b-f. Another robust feature is that the magnitude of
333 simulated rainfall during the JJAS period is also more in 2h31 and 24h31 than in 2h301 and
334 24h301 configurations and are in better agreement with the observational estimates. Similar
335 results are obtained if an Indian monsoon dynamical index is used instead of a rainfall time
336 series in the analysis (not shown) or if the rainfall indices are defined as the area-averaged
337 over all land-ocean or ocean only grid-points (see Table 3).

338 Further information on the seasonal cycle in the Indian areas is obtained by plotting
339 monthly SST means for the boxes used to compute the traditional IOD index as defined by
340 Saji et al. (1999). In the observations, the zonal SST gradient over the equatorial Indian Ocean
341 is negative throughout all the year, excepted in April during the transition between the winter
342 and summer monsoons (Fig. 5c). All the configurations are able to recover the shape of the
343 seasonal cycle of the Indian Ocean zonal SST gradient, but are affected by a strong positive
344 bias, which amplifies during late boreal summer and fall. Therefore, the simulated
345 climatological SST gradient is reversed compared to the observations. Moreover, this positive
346 bias is stronger when the vertical oceanic resolution is increased (e.g. 2h301 and 24h301).
347 This systematic error in the zonal SST gradient is due, on one hand, to a constant warm bias
348 in the western Indian Ocean throughout the seasonal cycle (see Fig. 5a) and, on the other
349 hand, to a cold bias in the eastern tropical Indian Ocean related to a shallower than observed
350 equatorial thermocline and increased evaporation during boreal summer and fall (see Fig. 5b).
351 The impact of the reversed SST zonal gradient on the IOD variability simulated by the
352 CGCM will be investigated in the next section.

353

354 (c) *Configurations differences*

355

356 The statistical significance of the differences among the boreal summer climatology in the
357 different experiments was estimated through a permutation test with 9999 shuffles (see Terray

358 et al. 2003 for more details) and one main conclusion of these computations is that none of
359 the differences between 2h31 (2h301) and 24h31 (24h301) SST, rainfall and surface wind
360 climatologies are statistically significant at the 90% confidence level according to this
361 permutation test (not shown). The comparison between the simulated climatologies has been
362 further extended to other quantities such as ocean temperature and winds at different levels.
363 Overall, all diagnostics confirm that the modification of the SST coupling frequency does not
364 substantially alter the CGCM climatology.

365 On the other hand, the use of an increased vertical oceanic resolution does change
366 significantly the modeled SST, rainfall and 850 hPa wind climatologies in the Pacific, as
367 illustrated in Figure 7 for 2h31 vs 2h301. Zonal SST gradient and the surface branch of the
368 Walker circulation along the equatorial Pacific are strengthened in 2h31 (24h31) compared to
369 2h301 (24h301). Consistently, the equatorial thermocline depth deepens in the western Pacific
370 and shoals in the eastern Pacific in 2h31 when compared to 2h301 (not shown). These
371 features explain why rainfall is increased over the western Pacific and the Maritime Continent
372 in 2h31 (24h31) in comparison to 2h301 (24h301) (Fig. 7b). Over the Indian sector, rainfall
373 average over India and the surface wind shear associated with the monsoon trough (over the
374 Indian subcontinent) are also increased in 2h31 (24h31) compared to 2h301 (24h301). Thus,
375 2h31 and 24h31 feature several indicators of significant differences toward a stronger
376 monsoon in its mean summer climate, which are in agreement with the enhanced Pacific trade
377 winds and Walker circulation. So, SINTEX-F2 exhibit some systematic differences when the
378 vertical oceanic resolution is increased, which may impact on the simulation of the ISM-
379 ENSO-IOD relationships and this will be investigated in the following section.

380 Surprisingly, the significant differences, which emerge between 2h31 (24h31) and 2h301
381 (24h301), also imply that, in many regions, the climatology's biases of the coupled model are
382 not necessarily reduced when the vertical oceanic resolution is increased.

383

384 **4. ENSO and IOD variability**

385

386 Prior to analyzing the ENSO-ISM and IOD-ISM relationships, we need to discuss the
387 statistical properties of ENSO and IOD in the different simulations.

388

389 (a) *Amplitude*

390

391 Standard-deviations of Niño-3.4 and IOD related bi-monthly (eg season of two months)
392 SST time series estimated from the four runs and the observations are shown in Table 2. 2h31
393 and 24h31 configurations have slightly larger Niño-3.4 SST variability than observed while
394 2h301 and 24h301 have slightly lower ENSO signal. This is consistent with the changes in
395 the mean state documented in Section 3, particularly, the strengthened Walker circulation and
396 the related modifications of SST gradient and thermocline depth in the equatorial Pacific in
397 2h31 and 24h31 configurations (e.g. when the vertical oceanic resolution is decreased). This
398 also suggests a plausible explanation for the increased Niño-3.4 SST variability in 2h31 and
399 24h31: the rise of the thermocline in the east found in 2h31 and 24h31 allows equatorial
400 upwelling to tap into sub-thermocline waters more easily for a given wind anomaly.

401 The standard deviation of the IOD index is much stronger in the four configurations than in
402 observations (see Table 2). It is also noticed that the eastern node of IOD (EIOD hereafter)
403 has greater interannual SST variability than the western node of IOD (WIOD hereafter) in all
404 the configurations, consistent with observations. However, the SST variability of EIOD is
405 also largely overemphasized compared to the observations as expected from the model biases
406 described in Section 3. The 2h31 and 24h31 runs also produce stronger interannual SST
407 variability in the equatorial Indian Ocean than 2h301 and 24h301, respectively (see Table 2).

408

409 Interestingly, the ENSO SST signal is also strengthened when 2-hourly SST coupling is
410 implemented instead of 1-day SST coupling and this result seems robust since it is verified for
411 both 31 and 301 vertical levels configurations of the CGCM (see Table 2).

412

413 (b) *Seasonal phase-locking*

414

415 Numerous studies have pointed out that the amplitude of ENSO and IOD cycles are
416 strongly phase-locked with the seasonal cycle (Chang et al., 2006). A good indicator of such
417 seasonal dependence is the monthly standard deviations of our Niño-3.4 and IOD indices
418 (Fig. 8). We have also plotted in this figure the monthly standard deviations of various
419 important indices for the evolution of the IOD such as the latent heat flux over EIOD and the
420 depth of the 20°C isotherm in the eastern equatorial Indian Ocean (Spencer et al., 2005).

421

422 The observations indicate significant phase-locking of Niño-3.4 SST variability to the
423 annual cycle, with weakest variability in April, and strongest in December-January (Fig. 8a).
424 These well-known results suggest that the transition periods between the opposite phases of

425 the ENSO cycle occurred in northern spring. 2h31 and 2h301 configurations capture
426 reasonably well the observed phase of ENSO, peaking in boreal winter. However, there is
427 also a tendency of the CGCM to produce a second peak of ENSO variability, during the early
428 boreal summer, which is not seen in the observations (Fig. 8a). As we will demonstrate later,
429 this bias is particularly detrimental to the simulation of the ISM-ENSO lead-lag relationships
430 in 24h31 and 24h301 configurations.

431

432 The monthly standard deviations of IOD and EIOD SST time series rise between May and
433 October when dipole events occurred and fall afterward in both observations and the different
434 simulations (Figs. 8b, d). However, IOD standard deviation in all months is much higher in
435 the CGCM and is mostly driven by the EIOD SST variability. The worst results are obtained
436 with the low vertical oceanic resolution, but also when 2-hourly SST coupling is implemented
437 (e.g. 2h31 and 2h301 configurations). Most of these changes in EIOD SST variability may be
438 related to the strength of the wind-evaporation-SST and wind-thermocline-SST feedbacks in
439 the eastern Indian Ocean (Li et al., 2003; Spencer et al., 2005; Fischer et al., 2005).

440 The maximum of interannual variability of latent heat flux or thermocline depth in the
441 eastern Indian Ocean is also anchored in the seasonal cycle; for the latent heat flux over EIOD
442 it is in the late boreal summer (August-September) and for the thermocline depth it arrives a
443 few months later in November (Figs. 8e-g). First, the differences between the model
444 configurations are far smaller than the errors relative to the observations. As an illustration,
445 the simulated latent heat flux variability is largely overemphasized in EIOD, but without any
446 clear differences with respect to the vertical oceanic resolution or the SST coupling frequency
447 (Fig. 8f).

448 Despite the large errors in the climatological thermocline depth (see Figs. 5d, e), the
449 seasonal cycle of thermocline depth variability in the equatorial eastern Indian Ocean (and off
450 Sumatra) is reproduced quite well in 2h31 and 2h301 configurations (e.g. when 2-hourly SST
451 coupling is used) with a maximum occurring in October-November, while 24h31 and 24h301
452 configurations have a tendency toward a much weaker thermocline variability, especially over
453 the equatorial eastern Indian Ocean (Figs. 8e, f). This may explain why 2h31 and 2h301 have
454 a higher EIOD SST variability than 24h31 and 24h301, respectively, during boreal fall
455 through the Bjerknes-type positive feedback (Fig. 8d). The differences in SST variability over
456 the eastern Indian Ocean between the twin experiments with increased oceanic resolution (e.g.
457 2h31-2h301 and 24h31-24h301) may be also related to changes in thermocline variability
458 over the eastern Indian Ocean, especially off Sumatra (Fig. 8f).

459 All these features are consistent with the results of Fischer et al. (2005) who show that the
460 wind-thermocline-SST positive feedback is an important dynamical mechanism at work in
461 IOD growth in the SINTEX model. However, since the thermocline standard-deviation in the
462 eastern equatorial Indian Ocean and off Sumatra is underestimated in the model, but the SST
463 and latent heat flux standard-deviations are both overestimated, the wind-evaporation-SST
464 feedback is probably also playing a key role in the simulated EIOD SST variability (Figs. 8d-
465 g).

466

467 (c) *Frequency*

468

469 Figure 9 shows the power spectra of Niño-3.4 SST and IOD time series from the model
470 experiments and the observations. Focusing first on the Niño-3.4 SST time series,
471 observations show a quite broad frequency peak between 3 and 5 yr. The 2h31 and 2h301
472 spectra are also significantly and strongly peaked at time scales around 4-5 years, while there
473 is a broader distribution of power across a range of frequencies both in 24h31 and 24h301.
474 Interestingly, the power spectra for 24h31 and 24h301 are near, or outside, the 99%
475 confidence interval of the observed Niño-3.4 SSTs power spectrum for frequencies
476 corresponding to the interannual time scale. Furthermore, 24h31 and 24h301 configurations
477 also miss the observed ratio between the energies associated with the annual cycle and the
478 interannual time scale which are thought to be important for a proper simulation of observed
479 ENSO variability (not shown; Guilyardi, 2006). In this respect, 2h31 and 2h301 spectra have
480 a highly realistic shape and dominant frequency, suggesting that the SST coupling frequency
481 plays an important role in making the ENSO signal in SINTEX-F2. On the other hand,
482 increasing the vertical oceanic resolution has only modest effects on spectral signature of the
483 simulated Niño-3.4 SSTs compared to the modifications induced by the 2-hourly SST
484 coupling.

485

486 Looking now to the IOD periodicity, observations suggests two main modes of
487 variability, e.g. the 4-7 years and biennial time scales. Consistent with the higher IOD
488 standard-deviations in 2h31 and 24h31 (see Fig. 8b), the 2h31 and 24h31 spectra are above
489 the upper 99% confidence limit estimated from the observations for frequencies in the
490 interannual range; however both are also able to reproduce the overall shape of the observed
491 spectrum. However, the diurnal SST coupling frequency has an impact in the simulated IOD
492 spectrum if we look at the high oceanic vertical resolution runs: the power between the two

493 preferred bands of IOD variability has been reduced whilst it is increased in each band for
494 2h301 compared to 24h301 (see Fig. 9d).

495

496 To further demonstrate the statistically significant effect of the diurnal SST coupling on
497 ENSO spectral characteristics, the log-ratios of power spectra for all the monthly SST time
498 series in the Indo-Pacific regions as simulated in the 2h31-24h31 and 2h301-24h301
499 experiments have been computed. These log-ratios have been squared and summed over the
500 range of frequencies corresponding to the interannual time scales (periods between 14 and 72
501 months) and the statistical significance of these sums has been tested against a Chi2
502 distribution (Fig. 10). More details on this Chi2 statistic and how to detect statistically
503 significant differences between two power spectra are given in Diggle (1990). Consistent with
504 our interpretation of the Niño-3.4 SST spectra, the power spectra of SST time series as
505 simulated by 2h31 and 2h301 are significantly different from those derived from 24h31 and
506 24h301, respectively, over large portions of the eastern and central Pacific and also in many
507 regions which are known to be largely influenced by ENSO through remote teleconnections
508 (e.g. the North and South Pacific, the South Indian Ocean, Alexander et al., 2002), confirming
509 that all the differences suggested above are robust and may affect remote regions through
510 atmospheric or oceanic pathways.

511

512 In summary, the amplitude of ENSO and IOD signals is decreased when the vertical
513 oceanic resolution is increased (e.g. in 2h301 and 24h301), probably through the changes of
514 the mean state documented in Section 3. The strength, frequency, and phase locking to the
515 annual cycle of El Niño are more realistic in the 2h31 and 2h301 configurations (e.g. with 2-
516 hourly SST coupling) than in the 24h31 and 24h301 configurations (e.g. with 1-day SST
517 coupling). Moreover, the seasonal phase-locking of eastern Indian Ocean SST or z20
518 variability is also improved with 2-hourly SST coupling, independently of the vertical oceanic
519 resolution used in the runs. We will now examine the possible impacts of these changes on
520 ISM and the ISM-ENSO-IOD relationships.

521

522 **5. ISM variability and ISM-ENSO-IOD relationships**

523

524 Numerous studies have pointed out the important role that ENSO and IOD play in
525 regulating ISM interannual variability and investigated the physical processes at the base of
526 the ISM-ENSO and ISM-IOD relationships using climate models (Ju and Slingo, 1995;

527 Ashok et al., 2004; Lau and Nath, 2004; Turner et al., 2005 ; Saji et al., 2006; Cherchi et al.,
528 2007; Terray et al., 2007; Bracco et al., 2007; Annamalai et al., 2007; Cai et al., 2009;
529 Krishnan et al., 2010). Yet, the difficulties associated with the coupled modeling of the
530 observed signal have received relatively less attention in the literature (Wu and Kirtman,
531 2005; Spencer et al., 2005; Turner et al., 2005; Terray et al., 2005b; Bracco et al., 2007). A
532 key issue is then to quantify to what extent the significant differences between the simulated
533 mean state when the oceanic resolution is increased (i.e. 2h301 and 24h301 configurations) or
534 the significant changes in ENSO characteristics when 2-hourly SST coupling is implemented
535 (i.e. 2h31 and 2h301 configurations) may improve the coupled simulation of ISM variability
536 and ISM-ENSO relationships in SINTEX (Terray et al., 2005b; Cherchi et al., 2007).

537

538 (a) *ISM interannual variability*

539

540 As a first measure of ISM variability in the different configurations, we define ISM rainfall
541 indices as the area-average of June to September (JJAS) rainfall anomalies over land, ocean
542 or land-ocean in the region 8° - 35° N and 65° - 95° E. The mean and standard-deviation of the
543 various ISM rainfall time series are compared with the observations in Table 3. 2h31
544 configuration is displaying both the higher mean rainfall and stronger variability. However,
545 no obvious systematic changes on rainfall variability are apparent when contrasting the
546 configurations with a modification of the vertical oceanic resolution or SST coupling
547 frequency. Overall, the variability of area-averaged ISM rainfall indices in the configurations
548 compares well with observations despite of the significant systematic errors in the mean state
549 described above.

550 To elucidate the temporal time scales involved in ISM rainfall variability, Figure 11 shows
551 the power spectra of ISM rainfall (over land) and normalized Niño-3.4 SST time series during
552 boreal summer (JJAS average) in observations and the different configurations. Interestingly,
553 the observed ISM rainfall time series is not basically biennial as it is assumed by many
554 studies (Yasunari, 1990; Meehl and Arblaster, 2002; Meehl et al., 2003), but rather exhibits a
555 quasi-triennial oscillation as many monsoon indicators (Bhalme and Jadhav, 1984). Focusing
556 now on the model's experiments, the results highlight that the dominant time scales of the
557 ISM rainfall indices have varied considerably and significantly between the 2h31 (2h301) and
558 24h31 (24h301) configurations. The ISM rainfall spectrum in 2h31 and 2h301 configurations
559 is strongly peaked at timescales between 2 and 6 years as the ENSO indices during boreal
560 summer. On the other hand, the ISM rainfall power spectrum in 24h31 or 24h301

561 configurations shows much decreased power across this range of frequencies and exhibits
562 more energy at very long periods. Moreover, the ISM rainfall power spectra of 2h31 and
563 2h301 are in reasonable and better agreement with the one estimated from the observations.
564 The log spectral ratios of ISM rainfall time series in the twin experiments 2h31-24h31 and
565 2h301-24h301 confirm the significant impact of 2-hourly SST coupling on the periodicity and
566 regularity of ISM rainfall indices (Figs. 11b, d). Furthermore, the corresponding results for
567 summer Niño-3.4 SSTs suggest that the improvements in ISM rainfall spectra simulated by the
568 2h31 and 2h301 configurations are linked to the fact that both versions of SINTEX-F2
569 perform better in their representation of ENSO and its spectral signature when compared with
570 the 24h31 and 24h301 configurations (Figs. 11.e-h).

571

572 (b) *ENSO-ISM relationships*

573

574 In order to corroborate this hypothesis, we now test the ability of SINTEX-F2 to reproduce
575 the observed relationships between ISM and ENSO by computing the lead-lag correlations
576 between the ISM rainfall (land-average over JJAS) and Niño-3.4 SST time series for all the
577 configurations and observations (AIR index is used) in a three years window from the
578 beginning of year -1 to the end of year +1, the year 0 referring to the year of the ISM season
579 (Fig. 12a).

580 The strong and significant negative correlation between ISM rainfall and SSTs over
581 eastern and central Pacific during boreal summer of year 0 implies that warmer (cooler) SSTs
582 over these regions will suppress (enhance) monsoon rainfall over India, a well-known
583 relationship (e.g. Webster et al., 1998; Wang et al., 2001). All the configurations of SINTEX-
584 F2 are able to reproduce this negative correlation between ISM rainfall and SSTs over eastern
585 and central Pacific during boreal summer (Fig. 12a). Consistent with the increased standard
586 deviation of Niño-3.4 SSTs (see Table 3) and the more energetic ENSO during boreal
587 summer when diurnal SST coupling is implemented (see Figs. 11.e-h), the magnitude of the
588 synchronous ISM-ENSO correlations is better simulated in the 2h31 and 2h301
589 configurations than in 24h31 and 24h301 experiments, respectively. Moreover, in the case of
590 24h31 and 24h301 configurations, the maximum negative correlation is just before the ISM
591 onset in May-June and the timing of the teleconnection is thus incorrect.

592 As can be clearly verified from Fig. 12a, the negative correlation between Niño-3.4 SSTs
593 and ISM rainfall occur only after boreal spring and the highest negative correlations are noted
594 during the late ISM and the following months. Surprisingly, the correspondence between the

595 model and the observations, as far as the ISM-Niño-3.4 SSTs lead-lag relationship is
596 concerned, is overall, very good and significantly improved *only when 2-hourly SST coupling*
597 *is implemented* (i.e. 2h31 and 2h301 configurations). Both in 2h31 and 2h301, the maximum
598 negative correlations for zero or slightly positive lags (i.e. for the ISM rainfall leading the
599 Niño-3.4 time series) are much better captured. This result suggests that the model’s ENSO in
600 its development stage remotely influences the ISM dynamics and leads to a substantial
601 reduction of ISM rainfall as in observations. Furthermore, the 2h31 configuration is also able
602 to recover the seasonal modulation of the monsoon-ENSO relationship with the rapid change
603 of sign of the correlations from positive to negative from year -1 to year 0 as observed. On the
604 other hand, both the 24h31 and 24h301 configurations share the same deficiencies as the other
605 CMIP3 coupled models exemplified in Fig.1, fail to reproduce the “spring predictability
606 barrier” of ENSO (Webster and Yang, 1992) and show significant negative correlations with
607 the Niño-3.4 SSTs *before rather than synchronous and after* the ISM. This common spurious
608 ENSO influence on ISM variability may be plausibly attributed to an incorrect phase-locking
609 of the model’s ENSO to the annual cycle as we will demonstrate below (i.e. anomalous
610 persistence of the model’s ENSO events during spring or too early onset of the events before
611 boreal spring).

612

613 We verified the independence of the preceding results on the observed dataset used and
614 choice of the ISM rainfall index by duplicating the correlation analyses of Fig. 12a, but with
615 the CMAP dataset and the ISM rainfall indices computed as land, ocean and land-averages
616 both from the observations and the different configurations of SINTEX-F2 (not shown). The
617 main results are analogous to what was previously described in the sense that the 2h31 and
618 2h301 configurations are more realistically simulating the ISM rainfall variability and its
619 relationship with ENSO, including the asymmetry in the lead-lag correlations and the spring
620 predictability barrier, while the two other configurations with 1-day SST coupling do not
621 capture the overall shape of the observed seasonal modulation of the ISM-ENSO relationship
622 and, especially, the spring barrier.

623 The property to capture the seasonal evolution of the correlations between monthly
624 Niño-3.4 SSTs and ISM rainfall is plausibly related to the ability of the 2h31 and 2h301
625 configurations to simulate correctly the space-time evolution of the SST anomalies and
626 associated diabatic heating anomalies during El Niño events (Turner et al., 2005; Annamalai
627 et al., 2007). Thus, we now focus on the SST patterns associated with Niño-3.4 SST time

628 series (Figures 13, 14 and 15) For the sake of brevity we show these diagnostics from only
629 two of the four model's configurations, but a similar correlation analysis has been
630 undertaken for the 2h301 and 24h301 configurations and we will also note any differences
631 between these runs and the twin experiments 2h31 and 24h31.

632 The correspondence between 2h31 (2h301) and the observations is striking during the
633 development stage of El Niño events. First, the observed correlation patterns before the El
634 Niño onset suggests the importance of extratropical latitudes, with possible precursory SST
635 signals stemming from the North Pacific and South Indian regions during February-March
636 (Terry et al., 2005a; Terry and Dominak, 2005; Terry et al., 2007; Vimont et al., 2003,
637 2009; Alexander et al., 2010). Interestingly, 2h31 is able to recover more precisely than
638 24h31, the SST precursory pattern found in the North Pacific region, which takes the form of
639 a warm C-shaped 'footprint' during AM both in observations and 2h31, consistent with
640 Vimont's "seasonal footprinting mechanism" (Vimont et al., 2003).

641 A clear ENSO signal is depicted with an eastward propagation of warm anomalies from
642 the west equatorial Pacific to the central and eastern Pacific from April-May to August-
643 September in both observations and the simulations. This eastward propagating SST signal is
644 characteristic of the observed ENSO evolution only after the so-called 1976/77 climate shift
645 (Wang, 1995; Trenberth and Stepaniak, 2001; Terry et Dominak, 2005; Guilyardi, 2006), but
646 it is dominating the correlation patterns when the computations are undertaken on the full
647 1950-2005 period. During the peak phase of ENSO, the tongue of positive correlations
648 extends too far west in the simulations, a bias also shared by many current CGCMs
649 (AchutaRao and Sperber, 2002, 2006). Moreover, this tongue of positive correlations is too
650 meridionally confined and the negative correlations forming the two branches of the
651 traditional horseshoe pattern are also split and much less intense in 24h31 (24h301) than in
652 the observations or 2h31 (2h301).

653 Model performance in the Indian Ocean is far from the success of the Pacific Ocean. As in
654 the period after the 1976/77 climate shift, El Niño (La Niña) onset is preceded by a basin-
655 wide Indian Ocean cooling (warming) in the simulations (Kug and Kang, 2006; Izumo et al.,
656 2008; Boschat et al., 2011a). However, the precursory SST subtropical dipole pattern in the
657 south Indian Ocean clearly visible during February-March in the observations (Terry and
658 Dominak, 2005; Terry, 2011; Yoo et al., 2010) is missing in our simulations. Next, the

659 observed positive correlations over the western Indian Ocean, increasing from June-July to
660 October-November (related to the weaker ISM circulation observed during summer of El
661 Niño developing year), are strongly polluted by the negative correlations extending from the
662 eastern equatorial Indian Ocean associated with a too strong IOD signal in the simulations.
663 But, once again, one can observe that this bias is much stronger in 24h31 (24h301) than 2h31
664 (2h301). Consistent with the existence of a significant IOD-ENSO relationship in SINTEX
665 (Gualdi et al., 2003; Fischer et al., 2005), positive correlations are simulated in the western
666 Indian Ocean and negative correlations in the eastern Indian Ocean during boreal fall by all
667 the configurations. However, these regional signals are much stronger than observed and
668 occurred too early, during boreal summer, in all the configurations, but especially in the
669 24h31 and 24h301 configurations. Finally, all the configurations reproduce the basin-wide
670 warming of the tropical Indian Ocean, which is observed when El Niño is mature, but this
671 warming is too weak in 24h31 (24h301). All these results highlight the positive impact of the
672 SST coupling frequency on the precursors and temporal evolution of ENSO at the Indo-
673 Pacific basin scale.

674

675 (c) *IOD-ISM relationships*

676 As in previous versions of the SINTEX model, all the integrations display a mode of
677 variability internal to the Indian Ocean with a dynamic comparable to the observed IOD (Fig.
678 8; see also Gualdi et al., 2003, Fischer et al., 2005; Behera et al., 2006). Maximum correlation
679 between ISM rainfall and monthly IOD occurs in September–November with an amplitude of
680 -0.3 (Fig. 12b). Interestingly, this season is also the period in which the ENSO–IOD
681 relationship is significant in the observations (Fischer et al., 2005; Behera et al., 2006). As is
682 clearly seen in Fig. 12b , the 2h301 and 24h301 configurations with increased vertical
683 oceanic resolution have problem in representing the teleconnections between ISM rainfall
684 and IOD during boreal summer of year 0. 24h31 configuration represents correctly some of
685 the features associated with the observed ISM-IOD relationship, but other aspects are less
686 well captured such as the tight phase-locking to the late boreal summer and fall season of
687 the correlations and spurious (significant) negative correlations before or near the ISM onset
688 are simulated. This is plausibly related to the too early IOD onset in 24h31 as discussed
689 above. The correlations are only realistically reproduced with the 2h31 configuration which
690 uses a reduced vertical oceanic resolution, but 2-hourly SST coupling. Overall, the vertical
691 oceanic resolution in the CGCM has a stronger (negative) impact than the SST coupling

692 frequency as far as the ISM-IOD relationships are concerned. Further work is needed to
693 understand the physical processes which are responsible of these important modifications in
694 the interannual variability of SINTEX-F2 in the Indian Ocean when changing the vertical
695 oceanic resolution.

696

697 **6. Conclusions**

698

699 There are numerous factors that may explain the current failure of CMIP3 coupled models
700 in simulating the observed ISM-ENSO relationship including 1) the models' ability to
701 simulate the mean Indo-Pacific climate, 2) the models' ability to simulate ENSO and 3) the
702 models' ability to simulate a realistic ENSO-ISM teleconnection (Annamalai et al., 2007).

703

704 Most CGCMs develop significant systematic errors in the mean state climate, particularly
705 in the monsoon circulation and precipitation, and there is currently little confidence in
706 seasonal forecasts or climate change projections due to the inaccuracies in CGCMs.
707 Eliminations of these biases are therefore highly desirable. Flux corrections methods have
708 been suggested as a practical method for improving the quality of seasonal and interannual
709 variability in CGCMs (Turner et al., 2005; Bracco et al., 2007; Manganello and Huang,
710 2009). As striking examples, the studies of Turner et al. (2005), Bracco et al. (2007) or
711 Manganello and Huang (2009) have demonstrated that improvement in representing the mean
712 state of the tropical Pacific through the use of flux adjustments gave rise to a more realistic
713 ENSO, which in turn improved the monsoon-ENSO relationship in coupled simulations.
714 However, the results from flux-corrected experiments may be model-dependent and are very
715 difficult to interpret due to the inconsistency of the climate model introduced by the flux
716 corrections (Spencer et al., 2007; Manganello and Huang, 2009).

717

718 In this study, as an alternative to flux corrections, the impacts of oceanic diurnal cycle on
719 the development of large-scale coupled phenomena such as ISM, IOD and ENSO are
720 investigated through the comparison of four different experiments using the same state-of-the-
721 art high resolution CGCM. In the first experiment (2h31), diurnal coupling is applied in the
722 CGCM by using 2-hourly coupling steps for all air-sea fluxes. A twin experiment (24h31)

723 using exactly the same CGCM, but with 1-day coupling frequency for the SST, has been
724 conducted in order to investigate whether diurnal SST high frequency variations may have an
725 effect on the simulated Indo-Pacific mean-state and variability. The interpretation of the
726 results is supported by a second ensemble with increased vertical oceanic resolution (e.g.
727 2h301 and 24h301 with 301 vertical levels in the ocean model). According to recent studies
728 (Danabasoglu et al., 2006; Bernie et al., 2008), the first two experiments (2h31 and 24h31)
729 with 31 vertical levels may not have a sufficient vertical resolution in the upper ocean to
730 allow a proper diurnal variability of the depth of the mixed layer, while the last two
731 experiments are able to capture this diurnal cycle of the mixed layer and may, consequently
732 have a more significant impact on the mean state and dynamics of the system through both
733 the diurnal rectification effect and other induced air-sea feedbacks (Ham et al., 2010). Despite
734 of this, the significant differences and improvements concerning the interannual variability of
735 the monsoon-ENSO system when comparing 2h31 to 24h31, on one hand, and 2h301 to
736 24h301 experiments, on the other hand, are very similar in many aspects.

737

738 As a first result, we found that increasing the vertical oceanic resolution in the CGCM has
739 a significant impact on the mean state, especially in the tropical Pacific, but that 2-hourly SST
740 coupling does not produce significant modulations of the background mean-state and seasonal
741 cycle in the tropics. However, when we moved to interannual variability, our simulations
742 point out to a reduction of coupled model biases when diurnal SST coupling is implemented,
743 independently of the vertical oceanic resolution used in the CGCM.

744

745 In agreement with our companion study (Masson et al., 2011), we found that ENSO
746 variability is very sensitive to diurnal SST coupling. In 2h31 and 2h301 experiments, Niño-3.4
747 SSTs have a larger standard deviation, a power spectrum with a sharper peak corresponding
748 to a 4-5 years oscillation and a more realistic evolution of tropical Pacific SST and associated
749 precipitation anomalies. Focusing on Indian Ocean variability, we found that the phase
750 locking to the annual cycle of eastern Indian Ocean SST and thermocline depth is also
751 improved as are the power spectra of ISM rainfall indices when 2-hourly SST coupling is
752 implemented. In other words, both 2h31 and 2h301 performed better in their representations
753 of ENSO and ISM variability when compared, respectively, with 24h31 and 24h301
754 experiments *without any significant changes in the basic state of the model*.

755

756 The different nature of ENSO in the model's configurations may obviously have a global
757 impact through remote teleconnections associated with the redistribution of latent heat
758 sources and sinks in the equatorial Pacific (Annamalai et al., 2007). The current work
759 confirms this hypothesis by demonstrating that the interannual variability of the whole
760 ENSO-ISM system is very sensitive to diurnal SST coupling. With 2-hourly SST coupling,
761 the simulation of the lead-lag relationships between ENSO and ISM is dramatically improved
762 and the CGCM is able to capture much better the spring predictability barrier, which is of
763 paramount importance for dynamical seasonal prediction of the monsoon. Related to the
764 stronger ISM-ENSO coupling, the spectrum of ISM rainfall variability is also shifted to
765 ENSO-related frequencies. This suggests that ISM in 2h31 and 2h301 configurations can
766 respond much more realistically to east Pacific SSTs once some of the systematic errors in
767 ENSO's evolution have been removed. On the other hand, the ISM-IOD teleconnection is
768 sensible to both diurnal SST coupling and the vertical oceanic resolution, but increasing the
769 vertical oceanic resolution is degrading the ISM-IOD teleconnection in the CGCM. In other
770 words, we suggest that the factors that are responsible for the more realistic simulation of the
771 ISM-ENSO-IOD relationships in our experiments with 2-hourly SST coupling can be traced
772 back to a large extent to significant changes in ENSO characteristics, such as its amplitude,
773 periodicity and evolution.

774

775 There have been already several studies devoted to the impact of the diurnal cycle on the
776 mean state, intraseasonal and interannual variability of the tropical system as simulated by
777 state-of-the-art CGCMs (Danabasoglu et al., 2006; Bernie et al., 2009; Ham et al., 2010).
778 According to these recent studies, diurnal air-sea coupling improve the performance of the
779 CGCMs by changing the climatology of the coupled model and producing a warmer mean
780 state which help to reduce the "cold tongue" bias in the equatorial Pacific by a mechanism
781 involving the diurnal variability of the mixed layer (Danabasoglu et al., 2006; Bernie et al.,
782 2009). These rectifications of the mean state may then modify both the intraseasonal and
783 interannual variabilities of the simulated system (Bernie et al., 2009; Ham et al., 2010).

784 However, if the diurnal oceanic cycle and the diurnal rectification mechanism of the mean
785 state has some role to play in our results, the robustness and similarity of the differences
786 between 2h31-24h31 and 2h301-24h301 configurations show that the diurnal oceanic cycle
787 forms only part of the explanation of the substantial changes in the nature of ENSO and
788 timing of the monsoon-ENSO teleconnections when 2-hourly SST coupling is implemented.
789 Moreover, these significant impacts on the behavior of El Niño and the associated

790 teleconnection patterns are not related to changes in the mean state of the coupled model in
791 our experiments, leaving open the question of other amplification mechanisms due
792 specifically to a more accurate air-sea coupling strategy. These differences between our
793 results and previous studies are obviously related to the fact that, in our experiments, all air-
794 sea fluxes other than SST are communicated using coupling steps of 2 hours, while other
795 studies have contrasted 1-day to 2-hourly coupling experiments for all the air-sea fluxes. This
796 leads to the hypothesis that other mechanisms must be at play for explaining our results, such
797 as a better simulation of temporal scale interactions when 2-hourly SST coupling is activated.
798 The implication of all these results, yet to be verified by a detailed analysis, is that large-scale
799 air-sea coupling and temporal scale interactions are prime mechanisms for the rectification of
800 the interannual variability of the coupled system in our coupled experiments instead of a
801 change of the mean state. Thus, our results emphasize the need for a better understanding of
802 the impact of the synoptic and intraseasonal time scales and their nonlinear scale interactions
803 with the interannual time scale as observed and simulated by CGCMs (Meehl et al., 2001).
804 The detailed analysis of these scale interactions in the tropical Indo-Pacific region in the
805 framework of our coupled model will be the subject of a forthcoming study. In any case, our
806 results highlight that air-sea coupling has to be represented as accurately as possible to
807 simulate the interannual variability of the ENSO-monsoon system and to correct present
808 model's deficiencies.

809 If we take into account that most of the CMIP3 coupled models fail to recover the complex
810 ISM-ENSO lead-lag relationships and produced similar results to the SINTEX-F2 model in
811 its 24h31 configuration, our results are intriguing. A plausible explanation for this general
812 failure is that most of the CMIP3 CGCMs still did not have the correct phase of ENSO with
813 respect to the annual cycle (Terray, 2006). The diversity in the simulation of ENSO variability
814 in the CMIP3 coupled models is still extremely high (Guilyardi, 2006), particularly with
815 respect to the phase-locking of ENSO on the annual cycle, and this shortcoming may
816 adversely affect the ability of the coupled models to simulate the monsoon-ENSO
817 teleconnection as seen in Fig. 1. However, it is also instructive to mention that a large
818 majority of the CMIP3 coupled models exchange atmospheric and oceanic parameters just
819 once a day. In such models, a poor representation of the diurnal air-sea coupling and related
820 scale interactions could also lead to errors than can be rectified into the interannual variability
821 of the system through non-linearities, even without any significant changes in the climatology
822 of the coupled model, as suggested by our results. Interestingly, three of four of the models

823 identified by Annamalai et al. (2007) that can successfully simulate the monsoon-ENSO
824 teleconnection also use 2-hourly coupling (see Fig. 1).

825 In conclusion, our study argues that important progress in simulating the interannual
826 variability of the tropical system can be achieved by modifications of the coupling strategies
827 currently used in CGCMs, without using any flux correction methods. Our model diagnostics
828 indicate that a proper simulation of the scale interactions embedded in the dynamics of the
829 climate system may also be a prerequisite to capture a realistic ISM-ENSO teleconnection, in
830 addition to a correct simulation of the basic state as suggested by others (Turner et al., 2005;
831 Annamalai et al., 2007). This emphasizes the need for a more detailed investigation of the
832 impact of coupling strategies on the simulation of Indo-Pacific interannual variability in
833 current CGCMs.

834 At the end, we want to emphasize that we do not argue that diurnal SST coupling will be
835 equally important in other state-of-the-art CGCMs and the results presented here may be
836 model-dependent. However, we do believe that coupling strategy is a relatively overlooked
837 area and may be more thoroughly diagnose in current CGCMs if further progress in the
838 simulation of the variability of the coupled climate system is to be achieved.

839 **Acknowledgments:** Financial support from the Indo-French CEFIPRA project (N° 3907/1)
840 and the European Community project ENSEMBLES (Project no. GOCE-CT-2003-505539) is
841 acknowledged. All the SINTEX-F2 experiments were carried out on the Earth Simulator
842 (JAMSTEC) in the frame of the France-Japan collaboration. Our sensibility experiments with
843 301 levels in the ocean have to be double thanks to the outstanding computational
844 performances offered by this unique supercomputer. S. Masson and G. Madec were supported
845 by ANR (INLOES project). Many thanks to R. Benshila, C. Talandier, A. Caubel, E.
846 Maisonnave, M.A. Foujols, C. Levy, Y.Meursedoif, F. Pinsard, C. Deltel, S. Denvil and P.
847 Brochard who have come to the ESC to implement, optimize and run the simulations. Their
848 visit at the ESC was greatly facilitated by the kind help of K. Takahashi, A. Kurita, R. Itakura,
849 A. Toya and M.-E. Demory. The NCEP-NCAR reanalysis, CMAP and HadISST1.1 data
850 were provided by the NOAA-CIRES Climate Diagnostics Center from the Web site
851 (<http://www.cdc.noaa.gov>). Finally, we acknowledge the outstanding work undertaken by the
852 many international modeling groups who provided their numerous model experiments for the
853 Program for Climate Model Diagnosis and Intercomparison (PCMDI). For more details on
854 model data or documentation, readers are referred to the PCMDI Web site ([http://www-](http://www-pcmdi.llnl.gov)
855 [pcmdi.llnl.gov](http://www-pcmdi.llnl.gov)).

856

857 **References**

858

859 Abram NJ, Gagan MK, Cole JE, Hantoro WS, Mudelsee M (2008) Recent intensification of
860 tropical climate variability in the Indian Ocean. *Nat. Geosci.* **1**, 849–853.

861

862 AchutaRao K, Sperber KR (2002) Simulation of the El Niño Southern Oscillation: Results from
863 the coupled model intercomparison project. *Climate Dyn.* **19**, 191–209.

864

865 AchutaRao KM, Sperber KR (2006) ENSO simulation in coupled ocean-atmosphere models:
866 Are the current models better? *Climate Dyn.*, **27**, 1–15.

867

868 Alexander MA, Bladé I, Newman M, Lanzante JR, Lau N-C, Scott JD (2002) The atmospheric
869 bridge: The influence of ENSO teleconnections on air–sea interaction over the global oceans.
870 *J. Climate*, **15**, 2205–2231.

871

872 Alexander MA, Vimont DJ, Chang P, Scott JD (2010) The impact of extratropical atmospheric
873 variability on ENSO: testing the Seasonal Footprinting Mechanism using coupled model
874 experiments. *J. Climate*, **23**, 2885–2901.

875

876 Annamalai H, Liu P (2005) Response of the Asian summer monsoon to changes in El Niño
877 properties. *Quart. J. Roy. Meteor. Soc.*, **131**, 805–831.

878

879 Annamalai H, Sperber KR (2005) Regional heat sources and the active and break phases of
880 boreal summer intraseasonal (30–50 day) variability. *J. Atmos. Sci.*, **62**, 2726–2748.

881

882 Annamalai H, Hamilton K, Sperber KR (2007) The South Asian summer monsoon and its
883 relationship with ENSO in the IPCC AR4 simulations. *J. Climate*, **20**, 1071–1092.

884

885 Ashok K, Guan Z, Yamagata T (2001) Influence of the Indian Ocean Dipole on the relationship
886 between the Indian monsoon rainfall and ENSO. *Geophys. Res. Lett.*, **28**, 4499–4502.

887

888 Ashok K, Guan Z, Saji NH, Yamagata T (2004) Individual and combined influences of ENSO
889 and the Indian Ocean Dipole on the Indian Summer Monsoon. *J. Climate*, **17**, 3141–3154.

890

891 Behera SK, Luo JJ, Masson S, Rao SA, Sakuma H (2006) A CGCM study on the interaction
892 between IOD and ENSO. *J. Climate*, **19**, 1688–1705.

893

894 Bernie DJ, Guilyardi E, Madec G, Slingo JM, Woolnough SJ (2007). Impact of resolving the
895 diurnal cycle in an ocean-atmosphere GCM. Part 1: a diurnally forced OGCM. *Climate Dyn.*,
896 **29**, 575–590.

897

898 Bernie DJ, Guilyardi E, Madec G, Slingo JM, Woolnough SJ, Cole J (2008) Impact of resolving
899 the diurnal cycle in an ocean--atmosphere GCM. Part 2: A diurnally coupled CGCM. *Climate
900 Dyn.*, **31**, 909–925.

901

902 Bhalme HN, Jadhav SK (1984) The Southern Oscillation and its relation to the monsoon
903 rainfall. *Int. J. of Climatology*, **4**, 509–520. DOI: 10.1002/joc.3370040506.

904
905 Boschat G, Terray P, Masson S (2011a) Interannual relationships between Indian Summer
906 Monsoon and Indo-Pacific coupled modes of variability during recent decades. *Clim. Dyn.*,
907 37:1019-1043, doi:10.1007/s00382-010-0887-y.
908
909 Boschat G, Terray P, Masson S (2011b) Robustness of SST teleconnections and precursory
910 patterns associated with the Indian Summer Monsoon. *Clim. Dyn.*, online,
911 doi:10.1007/s00382-011-1100-7.
912
913 Bracco A, Kucharski F, Molteni F, Hazeleger W, Severijns C (2007) A recipe for simulating the
914 interannual variability of the Asian summer monsoon and its relation with ENSO. *Clim. Dyn.*,
915 DOI: 10.1007/s000382-006-0190-0.
916
917 Cai W, Sullivan A, Cowan T (2009) Rainfall Teleconnections with Indo-Pacific variability in the
918 WCRP CMIP3 Models. *J. Climate*, **22**, 5046-5071.
919
920 Carton, JA, Giese BS, Grodsky SA (2005) Sea level rise and the warming of the oceans in the
921 SODA ocean reanalysis. *J. Geophys. Res.*, **110**, C09006, doi:10.1029/2004JC002817.
922
923 Chang C-P, Harr P, Ju J (2001) Possible Roles of Atlantic Circulations on the Weakening Indian
924 Monsoon Rainfall–ENSO Relationship. *J. Climate*, **14**, 2376–2380
925
926 Chang C-P and Coauthors (2006) Climate fluctuations of tropical coupled systems - The role
927 of ocean dynamics. *J. Climate*, **19**, 5122–5174.
928
929 Cherchi A, Gualdi S, Behera S, Luo JJ, Masson S, Yamagata T, Navarra A (2007) The influence
930 of tropical Indian Ocean SST on the Indian summer monsoon. *J. Climate*, **20**, 3083-3105.
931
932 Danabasoglu G, Large WG, Tribbia JJ, Gent PR, Briegleb BP, McWilliams JC (2006) Diurnal
933 coupling in the tropical oceans of CCSM3. *J. Climate*, **19**, 2347-365.
934
935 Diggle PJ (1990) Time series : a biostatistical introduction. Chapter 4, Clarendon Press,
936 Oxford.
937
938 Ebisuzaki W (1997) A method to estimate the statistical significance of a correlation when
939 the data are serially correlated. *J. Climate*, **10**, 2147-2153.
940
941 Fischer AS, Terray P, Delecluse P, Gualdi S, Guilyardi E (2005) Two Independent Triggers for
942 the Indian Ocean Dipole/Zonal Mode in a Coupled GCM. *J. Climate*, **18**, 3428–3449.
943
944 Gadgil S, Rajeevan M, Nanjundiah R (2005) Monsoon prediction - why yet another failure?
945 *Curr. Sci.*, **84**, 1713-1719.
946
947 Gershunov A, Schneider N, Barnett T (2001) Low-frequency modulation of the ENSO-Indian
948 monsoon rainfall relationship: signal or noise? *J. Climate*, **14**, 2486-2492.
949

950 Goswami BN, Wu G, Yasunari T (2006) Annual cycle, Intraseasonal Oscillations and
 951 Roadblock to seasonal predictability of the Asian summer monsoon. *J. Climate*, **19**, 5078-
 952 5099.

953

954 Gualdi, S, Guilyardi E, Navarra A, Masina S, Delecluse P (2003) The interannual variability in
 955 the tropical Indian Ocean as simulated by a CGCM. *Clim. Dyn.*, **20**, 567-582.

956

957 Guilyardi E (2006) El Niño-mean state--seasonal cycle interactions in a multi-model
 958 ensemble. *Clim. Dyn.*, **26**, 329-348.

959

960 Guilyardi E, Delecluse P, Gualdi S, Navarra, A (2003) Mechanisms for ENSO phase change in a
 961 coupled GCM. *J. Climate*, **16**, 1141-158.

962

963 Guilyardi E, Wittenberg, A, Fedorov A, Collins M, Wang C (2009) Understanding El Niño in
 964 ocean-atmosphere general circulation models. *Bull. Amer. Meteor. Soc.*, **90**, 325-340.

965

966 Ham YG, Kug JS, Kang IS, Jin FF, Timmermann A (2010) Impact of diurnal atmosphere--ocean
 967 coupling on tropical climate simulations using a coupled GCM. *Clim. Dyn.*, **34**, 905-917.

968

969 Izumo T, de Boyer Montégut C, Luo J-J, Behera SK, Masson S, Yamagata T (2008) The role of
 970 the western Arabian Sea upwelling in Indian monsoon rainfall variability, *J. Climate*, **21**,
 971 5603-5623.

972

973 Joseph R, Nigam S (2006) ENSO evolution and teleconnection in IPCC's twentieth-century
 974 climate simulations: Realistic representation? *J. Climate*, **19**, 4360–4377.

975

976 Ju J, Slingo JM (1995) The Asian summer monsoon and ENSO. *Quart. J. Roy. Meteor. Soc.*,
 977 **121**, 1133-1168.

978

979 Kalnay E, Kanamitsu M, Kistler R, Collins W, Deaven D, Gandin L, Iredell M, Saha S, White G,
 980 Woollen J, Zhu Y, Chelliah M, Ebisuzaki W, Higgins W, Janowiak J, Mo KC, Ropelewski C,
 981 Wang J, Leetmaa A, Reynolds R, Jenne R, Joseph D (1996) The NCEP/NCAR 40-year reanalysis
 982 project. *Bull. Amer. Met. Soc.*, **77**, 437-471.

983

984 Kawai Y, Wada A (2007) Diurnal sea surface temperature variation and its impact on the
 985 atmosphere and ocean: a review. *Journal of Oceanography*, **63**, 721-744.

986

987 Kinter JL, Miyakoda K, Yang S (2002) Recent change in the connection from the Asian
 988 Monsoon to ENSO. *J. Climate*, **15**, 1203–1215.

989

990 Krishna Kumar K, Rajagopalan B, Cane M (1999) On the Weakening Relationship Between
 991 the Indian Monsoon and ENSO, *Science*, **284**, 2156-2159.

992

993 Krishna Kumar K, Hoerling M, Rajagopalan B (2005) Advancing dynamical prediction of
 994 Indian monsoon rainfall, *Geophys. Res. Lett.*, **32**, 1-4.

995

996 Krishna Kumar, K. et al. (2006) Unravelling the Mystery of Indian Monsoon Failure During El
 997 Niño. *Science* 314, 115; DOI: 10.1126/science.1131152.

998

999 Krishnamurthy, V., et B.N. Goswami, 2000: Indian monsoon-ENSO relationship on inter
1000 decadal time scales. *J. Climate*, **13**, 579-595.

1001

1002 Krishnan R, Swapna P (2009) Significance influence of the boreal summer monsoon flow on
1003 the Indian Ocean response during dipole events. *J. Climate*, **22**, 5611-5634.

1004

1005 Krishnan R, Sundaram S, Swapna P, Kumar V, Ayantika DC, Mujumdar M (2010) The crucial
1006 role of ocean-atmosphere coupling on the Indian monsoon anomalous response during
1007 dipole events. *Clim. Dyn.*, DOI: 10.1007/s00382-010-0830-2

1008

1009 Kucharski F, Bracco A, Yoo JH, Molteni F (2007) Low-frequency variability of the Indian
1010 Monsoon-ENSO relation and the Tropical Atlantic; The 'weakening' of the 1980s and 1990s.
1011 *J. Climate*, **20**, 4255-4266.

1012

1013 Kucharski F, Bracco A, Yoo JH, Molteni F (2008) Atlantic forced component of the Indian
1014 monsoon interannual variability. *Geophys. Res. Lett.*, **35**, L04706.
1015 doi:10.1029/2007GL033037.

1016

1017 Kug JS, Kang I-S (2006) Interactive feedback between ENSO and the Indian Ocean. *J. Climate*,
1018 **19**, 1784-1801.

1019

1020 Lau NC, Nath MJ, (2004) Coupled GCM Simulation of Atmosphere–Ocean Variability
1021 Associated with Zonally Asymmetric SST Changes in the Tropical Indian Ocean. *J. Climate*, **17**,
1022 245-265

1023

1024 Li T, Wang B, Chang CP, Zhang YS (2003) A theory for the Indian Ocean Dipole-Zonal Mode. *J.*
1025 *Atmos. Sci.*, **60**, 2119–2135.

1026

1027 Li T, Liu P, Fu X, Wang B, Meehl GA (2006) Spatial-temporal structure of tropical biennial
1028 oscillation. *J. Climate*, **19**, 3070-3087.

1029

1030 Lindzen RS, Nigam S (1987) On the role of sea surface temperature gradients in forcing low-
1031 level winds and convergence in the Tropics. *J. Atmos. Sci.*, **44**, 2418-2436.

1032

1033 Loschnigg J, Meehl GA, Arblaster JM, Compo GP, Webster PJ (2003) The Asian monsoon, the
1034 tropospheric biennial oscillation, and the Indian Ocean dipole in the NCAR CSM. *J. Climate*,
1035 **16**, 1617-1642.

1036

1037 Luo JJ, Masson S, Behera S, Delecluse P, Gualdi S, Navarra A, Yamagata T (2003) South Pacific
1038 origin of the decadal ENSO-like variation as simulated by a coupled GCM. *Geophys. Res. Lett.*,
1039 **30**, 2250-2254.

1040

1041 Luo JJ, Masson S, Roeckner E, Madec G, Yamagata T (2005) Reducing climatology bias in an
1042 ocean--atmosphere CGCM with improved coupling physics. *J. Climate*, **18**, 2344-360.

1043

1044 Madec G (2008) "NEMO ocean engine". Note du Pole de modélisation, Institut Pierre-Simon
1045 Laplace (IPSL), France, No 27 ISSN No 1288-1619.

1046

1047
1048 Madec G, Delecluse P, Imbard M, Lévy C (1998) OPA 8.1 Ocean General Circulation Model
1049 reference manual. Note du Pole de modélisation, Institut Pierre-Simon Laplace (IPSL),
1050 France, N°11, 91pp.
1051
1052 Manganello JV, Huang B (2009) The influence of systematic errors in the Southeast Pacific on
1053 ENSO variability and prediction in a coupled GCM. *Clim. Dyn.*, 32, 1015-1034, DOI
1054 10.1007/s00382-008-0407-5.
1055
1056 Masson S, Terray P, Madec G, Luo JJ, Yamagata T, Takahashi K (2011) Impact of intra-daily
1057 SST variability on ENSO characteristics in a coupled model. Submitted to *Climate Dynamics*.
1058
1059 Meehl GA, Lukas R, Kiladis GN, Wheeler M, Matthews A, Weickmann KM (2001) A
1060 conceptual framework for time and space scale interactions in the climate system. *Clim.*
1061 *Dyn.*, **17**, 753–775.
1062
1063 Meehl GA, Arblaster J (2002) The tropospheric biennial oscillation and the Asian-Australian
1064 monsoon rainfall. *J. Climate*, **15**, 722-744.
1065
1066 Meehl GA, Arblaster JM, Loschnigg J (2003) Coupled Ocean-Atmosphere Dynamical
1067 Processes in the Tropical Indian and Pacific Oceans and the TBO. *J. Climate*, **16**, 2138-2158.
1068
1069 Meehl, G. A. et al. (2007) The WCRP CMIP3 multi-model dataset: a new era in climate
1070 change research. *Bull. Am. Met. Soc.*, 88: 1383-1394.
1071
1072 Molines JM, Barnier B, Penduff T, Brodeau L, Treguier AM, Theetten S, Madec G (2006),
1073 Definition of the global 1/2° experiment with CORE interannual forcing, ORCA05-G50. LEGI
1074 report, November 2006. LEGI-DRA-1-11-2006,
1075 http://www.ifremer.fr/lpo/drakkar/drakkar/configs/ORCA05/orca05_G50.pdf.
1076
1077 Nordeng TE (1994) Extended versions of the convective parameterization scheme at
1078 ECMWF and their impact on the mean and transient activity of the model in the tropics,
1079 Tech. Memo. 206, Eur. Cent. for Medium-Range Weather Forecasts, Reading, UK.
1080
1081 Palmer TN, et Coauthors (2004) Development of an European multi-model ensemble system
1082 for seasonal to interannual prediction (DEMETER). *Bull. Am. Met. Soc.*, **85**, 853-872.
1083
1084 Parthasarathy B, Munot AA, Kothawale DR (1994) All-India monthly and seasonal rainfall
1085 series: 1871–1993. *Theor. Appl. Climatol.* **49**, 217–224.
1086
1087 Rayner NA, Parker DE, Horton EB, Folland CK, Alexander LV, Rowell DP, Kent EC, Kaplan A
1088 (2003) Global analyses of sea surface temperature, sea ice, and night marine air temperature
1089 since the late nineteenth century. *J. Geophys. Res.*, 108(D14)4407. doi:
1090 10.1029/2002JD002670.
1091
1092 Reichler T, and Kim J (2008). How well do coupled models simulate today's climate? *Bull.*
1093 *Am. Met. Soc.*, **89**, 303-311.
1094

1095 Roeckner E, et Coauthors (1996) The atmospheric general circulation model ECHAM-4:
1096 model description and simulation of present-day climate. Max-Planck-Institut für
1097 Meteorologie, report n°218, 94pp.
1098

1099 Roeckner E, Bäuml G, Bonaventura L, Brokopf R, Esch M, Giorgetta M, Hagemann S,
1100 Kirchner I, Kornblueh L, Manzini E, Rhodin A, Schlese U, Schulzweida U, Tompkins A
1101 (2003) The atmospheric general circulation model ECHAM 5. PART I: Model description. MPI-
1102 Report 349.
1103

1104 Roeckner E, Brokopf R, Esch M, Giorgetta M, Hagemann S, Kornblueh L, Manzini E, Schlese U,
1105 Schulzweida U (2004) The atmospheric general circulation model ECHAM5 Part II: Sensitivity
1106 of simulated climate to horizontal and vertical resolution. Max-Planck-Institute for
1107 Meteorology, MPI-Report 354.
1108

1109 Saji NH, Goswami BN, Vinayachandran PN, Yamagata TA (1999) Dipole Mode in the Tropical
1110 Indian Ocean. *Nature*, **401**, 360–363.
1111

1112 Saji NH, Xie S-P, Yamagata T (2006) Tropical Indian Ocean variability in the IPCC twentieth-
1113 century climate simulations. *J. Climate*, **19**, 4397–4417. DOI: 10.1175/JCLI3847.1.
1114

1115 Slingo J, Inness P, Neale R, Woolnough S, Yang G (2003) Scale interactions on diurnal to
1116 seasonal timescales and their relevance to model systematic errors. *Annals of Geophysics*,
1117 **46**, 139-155.
1118

1119 Spencer H, Sutton RT, Slingo JM, Roberts M, Black E (2005) Indian Ocean Climate and Dipole
1120 Variability in Hadley Centre Coupled GCMs. *J. Climate*, **18**, 2286-2307.
1121

1122 Spencer H, Sutton RT, Slingo JM (2007) El Niño in a Coupled Climate Model: Sensitivity to
1123 Changes in Mean State Induced by Heat Flux and Wind Stress Corrections. *J. Climate*, **20**,
1124 2273-2273.
1125

1126 Terray P, Delecluse P, Labattu S, Terray L (2003) Sea Surface Temperature Associations with
1127 the Late Indian Summer Monsoon. *Clim. Dyn.*, **21**, 593–618.
1128

1129 Terray P, Dominiak S (2005) Indian Ocean Sea Surface Temperature and El Niño-Southern
1130 Oscillation: a new perspective. *J. Climate*, **18**, 1351-1368.
1131

1132 Terray P, Dominiak S, Delecluse P (2005a) Role of the southern Indian Ocean in the
1133 transitions of the monsoon-ENSO system during recent decades. *Clim. Dyn.*, **24**, 169-195,
1134 DOI: 10.1007/s00382-004-0480-3.
1135

1136 Terray P, Guilyardi E, Fischer AS, Delecluse P (2005b) Dynamics of the Indian Monsoon and
1137 ENSO Relationships in the SINTEX global Coupled Model. *Clim. Dyn.*, **24**, 145-168.
1138

1139 Terray P (2006) Assessment of the representation of monsoon and its teleconnection with
1140 the ocean variability from IPCC scenarios with the European models. European ENSEMBLES
1141 project (Project no. GOCE-CT-2003-505539). Deliverable D.5.17, 20 pp.
1142

1143 Terray P, Chauvin F, Douville H (2007) Impact of southeast Indian Ocean Sea Surface
1144 Temperature anomalies on monsoon-ENSO-dipole variability in a coupled ocean-atmosphere
1145 model. *Clim. Dyn.*, **28**, 553-580. doi:10.1007/s00382-006-0192-y
1146

1147 Terray P (2011) Southern Hemisphere extra-tropical forcing: a new paradigm for El Niño-
1148 Southern Oscillation. *Clim. Dyn.*, 36:2171-2199, doi:10.1007/s00382-010-0825-z.
1149

1150 Tiedtke M (1989). A comprehensive mass flux scheme for cumulus parameterization in large-
1151 scale models. *Mon. Weather Rev.*, **117**, 1779-1800.
1152

1153 Timmermann R, Goosse H, Madec G, Fichefet T, Etche C, Duliere C (2005) On the
1154 representation of high latitude processes in the ORCA-LIM global coupled sea-ice-ocean
1155 model. *Ocean Modell.*, **8**, 175–201.
1156

1157 Trenberth KE, Stepaniak DP (2001) Indices of El Niño evolution. *J. Climate*, **14**, 1697–1701.
1158

1159 Turner AG, Inness PM, Slingo JM (2005) The role of the basic state in the ENSO-monsoon
1160 relationship and implications for predictability. *Quart. J. Roy. Meteor. Soc.*, **131**, 781–804.
1161

1162 Valcke S (2006) OASIS3 User Guide (prism_2-5). PRISM Support Initiative Report No 3, 64pp
1163

1164 Vimont DJ, Wallace JM, Battisti DS (2003) The seasonal footprinting mechanism in the
1165 Pacific: Implications for ENSO. *J. Climate*, **16**, 2668–2675.
1166

1167 Vimont DJ, Alexander M, Fontaine A (2009) Midlatitude Excitation of Tropical Variability in
1168 the Pacific: The Role of Thermodynamic Coupling and Seasonality. *J. Climate*, **22**, 518-534.
1169

1170 Wang B (1995) Interdecadal changes in El Niño onset in the last four decades. *J. Climate*, **8**,
1171 267-285.
1172

1173 Wang B (2006) The Asian Monsoon. Springer- Verlag/Praxis Publishing, New York, 787 pp.
1174

1175 Wang B, Wu R, Lau K-M (2001) Interannual Variability of the Asian Summer Monsoon:
1176 Contrasts between the Indian and the Western North Pacific–East Asian Monsoons. *J.*
1177 *Climate*, **14**, 4073-4090.
1178

1179 Wang B, Ding Q, Fu X, Kang I-S, Jin K, Shukla J, Doblus-Reyes F (2005) Fundamental
1180 challenges in simulation and prediction of summer monsoon rainfall, *Geophys. Res. Lett.*, **32**,
1181 L15711,doi: 10.1029/2005GL022734 12.
1182

1183 Webster PJ, Magana VO, Palmer TN, Shukla J, Tomas RA, Yanai M, Yasunari T (1998)
1184 Monsoons: Processes, predictability and the prospects for prediction. *J. Geophys. Res.*,
1185 103(C7):14 451–14 510.
1186

1187 Webster PJ, Yang S (1992) Monsoon and ENSO: Selectively interactive systems. *Quart. J. Roy.*
1188 *Meteor. Soc.*, **118**, 877-926.
1189

1190 Welch PD (1967) The use of Fast Fourier Transform for the estimation of power spectra: a
1191 method based on time averaging over short, modified periodograms. *IEEE Transactions on*
1192 *Audio and Electroacoustics*, **15**, 70-73.
1193
1194 Wu R, Kirtman BP (2003) On the impacts of Indian summer monsoon on ENSO in a coupled
1195 GCM. *Quart. J. Roy. Meteor. Soc.*, **129**, 3439–3468.
1196
1197 Wu R, Kirtman BP (2005) Role of Indian and Pacific Ocean air-sea coupling in tropical
1198 atmospheric variability. *Clim. Dyn.*, **25**, 155-179.
1199
1200 Wu R, Kirtman BP (2007) Role of Indian Ocean in the biennial transition of the Indian
1201 summer monsoon. *J. Climate*, **20**, 2147-2164.
1202
1203 Wu R, Kirtman BP, Pegion K (2006) Local air-sea relationship in observations and model
1204 simulations. *J. Climate*, **19**, 4914-4932.
1205
1206 Wu R, Kirtman BP (2007) Regimes of local air-sea interactions and implications for
1207 performance of forced simulations. *Clim. Dyn.*, **29**, 393-410.
1208
1209 Xavier, P. K., Marzin, C. and Goswami, B. N. (2007) An objective definition of the Indian
1210 summer monsoon season and a new perspective on the ENSO-monsoon relationship. *Quart.*
1211 *J. Roy. Meteor. Soc.*, **133**: 749-764.
1212
1213 Xie P, Arkin PA (1997) Global precipitation: A 17-year monthly analysis based on gauge
1214 observations, satellite estimates and numerical model outputs. *Bull. Amer. Meteor. Soc.*, **78**,
1215 2539-2558.
1216
1217 Yasunari T (1990) Impact of Indian monsoon on the coupled atmosphere/ocean system in
1218 the tropical Pacific. *Meteor. & Atmos. Phys.*, **44**, 29-41.
1219
1220 Yoo SH, Fasullo J, Yang S, Ho CH (2010) On the relationship between Indian Ocean sea
1221 surface temperature and the transition from El Niño to La Niña. *J. Geophys. Res.*, **115**,
1222 D15114, doi:10.1029/2009JD012978.
1223
1224 Yu L, Jin X, Weller RA (2008) Multidecade Global Flux Datasets from the Objectively Analyzed
1225 Air-sea Fluxes (OAFlux) Project: Latent and sensible heat fluxes, ocean evaporation, and
1226 related surface meteorological variables. Woods Hole Oceanographic Institution, *OAFlux*
1227 *Project Technical Report*. OA-2008-01, 64pp. Woods Hole. Massachusetts.
1228
1229
1230
1231

1232 **Figure captions**

1233 **Figure 1:** Lead-lag correlations between the ISM rainfall and the monthly Niño-3.4 SSTs
1234 (SST averaged over 5°S–5°N, 170°–120°W) starting several months before the onset of the
1235 monsoon (January) and finishing several months after the withdrawal of the monsoon
1236 (December) in the twentieth century runs (20c3m) of the CMIP3 from 20 different state-of-
1237 the-art coupled models and observational estimates. All the correlation coefficients are
1238 estimated from the 1870-2000 period both for observations and 20c3m simulations after
1239 detrending the SST time series. For each of the models one realization (the first) of the
1240 twentieth-century simulations were used to evaluate the ISM-ENSO relationship.

1241 **Figure 2:** (a) SST boreal summer climatology as derived from the HadISST dataset and
1242 estimated from the 1958-2008 period (b) (c) (d) (e) differences with the SST climatologies of
1243 2h31, 24h31, 2h301 and 24h301, respectively.

1244 **Figure 3:** Same as Figure 2, but for the rainfall climatology estimated from CMAP on the
1245 1979-2008 period. Differences between the GPCP and CMAP boreal summer rainfall
1246 climatologies are also shown in Fig. 3b.

1247 **Figure 4:** Same as Figure 2, but for the 850 hPa wind climatology estimated from NCEP
1248 reanalysis on the 1979-2008 period.

1249 **Figure 5:** (a) Climatological annual cycle of SST averaged over the eastern node of IOD
1250 (15°S-0°, 85°-110°E) computed from the HadISST dataset and the four SINTEX-F2
1251 configurations (b) Same as (a), but for the western node of IOD (15°S-10°N, 50°-75°E) (c)
1252 Climatological annual cycle of the IOD index from observations and the four configurations
1253 (d) Climatological annual cycle of the depth of the 20°C isotherm averaged over the eastern
1254 equatorial Indian Ocean (2°S-2°N, 90°-100°E) computed from SODA and the four
1255 configurations (e) Same as (d), but for the depth of 20°C over the Sumatra region (10°-2°S,
1256 95°-105°E) (f) Climatological annual cycle of latent heat flux averaged over the eastern node
1257 of IOD computed from OAFLUX dataset (Yu et al., 2008) and the four configurations of
1258 SINTEX-F2.

1259 **Figure 6:** Mean annual cycle of rainfall averaged over the Indian subcontinent (land grid
1260 points between 8-35°N and 65-95°E) for the observations (CMAP dataset) and the coupled
1261 model simulations.

1262 **Figure 7:** (a) Differences between the boreal summer SST climatologies of the 2h31 and
1263 2h301 configurations (b) Same as (a), but for the rainfall climatologies (c) Same as (a), but for
1264 the 850 hPa wind climatologies. In panels (a) and (b), the differences which are significant at
1265 the 95% confidence level are underlined. In panel (c), the map only show 850 hPa wind
1266 differences which are above the 95% confidence level. These confidence levels have been
1267 assessed using a permutation procedure with 9999 shuffles; see Terray et al. (2003) for more
1268 details.

1269 **Figure 8:** (a) Monthly standard deviations of the Niño-3.4 SST time series from HadISST
1270 dataset and the four configurations (b) Same as (a), but for the IOD index (c) Same as (a), but
1271 for western node IOD (15°S-10°N, 50°-75°E) SST time series (d) Same as (a), but eastern
1272 node IOD (15°S-0°, 85°-110°E) SST time series (e) Monthly standard deviations of the depth

1273 of the 20°C isotherm averaged over the eastern equatorial Indian Ocean (2°S-2°N, 90°-100°E)
1274 computed from SODA and the four configurations (e) Same as (d), but for the depth of 20°C
1275 over the Sumatra region (10°-2°S, 95°-105°E) (f) Monthly standard deviations of latent heat
1276 flux averaged over the eastern node of IOD computed from OAFLUX dataset (Yu et al.,
1277 2008) and the four configurations of SINTEX-F2.

1278 **Figure 9:** (a) Power spectra of seasonally adjusted and detrended bi-monthly Niño-3.4 SST
1279 time series for observations (black line) 2h31 (red line) and 24h31 (green line) configurations
1280 (b) Same as (a) but for 2h301 (red line) and 24h301 (green line) configurations (c) Same as
1281 (a), but for the IOD index (d) Same as (b), but for the IOD index. The bottom axis of each
1282 panel is the period (unit: year), the left axis is variance (unit: °C²) and both axes are in
1283 logarithm scale. The power spectrum is estimated using a FFT algorithm on overlapping
1284 segments (Welch, 1967) and the 99% confidence interval for the spectra estimated from the
1285 observations is plotted in black dashed lines in each panel.

1286 **Figure 10:** (a) Sum of squared log-ratios of the power spectral densities (Chi2 statistic) of
1287 2h31 and 24h31 grid-point SST time series over the Indo-Pacific region (color shading) for
1288 the periods between 14.4 and 72 months and associated 90% confidence level for testing the
1289 hypothesis of a common spectrum for the two estimated spectra between 2h31 and 24h31 (b)
1290 Same as in (a), but for the 2h301 and 24h301 configurations.

1291 **Figure 11:** (a) Normalized power spectra of ISM rainfall time series for observations (black
1292 line) 2h31 (red line) and 24h31 (green line) configurations. The bottom axis is the period
1293 (unit: year), the left axis is variance (unit: (mm/day)²) and both axes are in logarithm scale.
1294 The power spectrum is estimated using a FFT algorithm on overlapping segments (Welch,
1295 1967) and the 99% confidence interval for the spectra estimated from the observations is
1296 plotted in black dashed lines (b) Logarithm of the ratio of the power spectra of 2h31 and
1297 24h31 and point-wise 90% confidence intervals for the logarithms of the spectral ratios for a
1298 postulated common spectrum of the ISM rainfall time series in 2h31 and 24h31 (c) and (d)
1299 Same as (a) and (b), respectively, but for the 2h301 and 24h301 configurations. (e), (f), (g)
1300 and (h) Same as (a), (b), (c) and (d), respectively, but for the boreal summer (JJAS) Niño-3.4
1301 SST time series.

1302 **Figure 12:** (a) Lead-lag correlations between ISM rainfall and monthly Niño-3.4 for
1303 observations (black line), 2h31 (blue line), 24h31 (green line), 2h301 (yellow line) and
1304 24h301 (red line) configurations of SINTEX-F2, starting from the beginning of the previous
1305 year (e.g. year -1) to the end of the following year of the monsoon (e.g. year +1). IITM
1306 rainfall and HadISST datasets for the period 1900-2005 are used to estimate the correlation
1307 coefficients. X-axis indicates calendar month for a 36 months period starting one year before
1308 the developing year of ISM and Y-axis is the amplitude of the correlation. Thus, the
1309 coefficients corresponding to -1, 0, +1 month lags refer, respectively, to the correlations
1310 between (JJAS) ISM rainfall in year 0 and may, june and july Niño-3.4 SST index, also
1311 during year 0, and so on. (b) Same as (a) but, between ISM rainfall and the monthly IOD
1312 index. Diamond symbols indicate correlations that are above the 95% significance confidence
1313 level according to a phase-scramble bootstrap test (Ebisuzaki, 1997).

1314 **Figure 13:** Lagged correlations between bi-monthly averaged Indo-Pacific SSTs and the
1315 December-January Niño-3.4 SST for the HadISST. The correlations are calculated beginning

1316 in February-March, prior to the El Niño onset, and ending in December-January at the peak
1317 season of El Niño events. Correlations that are above the 95% significance confidence level
1318 according to a phase-scramble bootstrap test (Ebisuzaki, 1997) are underlined.

1319 **Figure 14:** Same as Fig. 13, but for 2h31 configuration.

1320 **Figure 15:** Same as Fig. 13, but for 24h31 configuration.

1321

1322

1323 **Table captions**

1324

1325 **Table 1:** Summary of the numerical experiments with their main characteristics, including
1326 length, horizontal and vertical resolutions and frequency of coupling for the different air-sea
1327 fluxes.

1328

1329 **Table 2:** Standard-deviations (in °C) of Niño-3.4, IOD, Eastern (EIOD) and Western (WIOD)
1330 nodes of IOD bi-monthly SST time series in the four runs and HadISST dataset (1958-2008).
1331 These values are computed after the removal of the long-term mean annual cycle and the
1332 contribution of timescales longer than 20 years.

1333

1334 **Table 3:** Comparison of means and standard-deviations (in mm/day) of ISM rainfall in the
1335 SINTEX runs and CMAP (period 1979-2008) for land only, land-sea and ocean only averages
1336 in the domain 8°-35°N and 65°-95°E.

1337

1338

1339

1340

1341

1342

1343 **Table 1**

Experience name	2h31	24h31	2h301	24h301
Oceanic vertical resolution	31 (10m)	31 (10m)	301 (1m)	301 (1m)
SST coupling frequency	2h	24h	2h	24h
Other data coupling frequency	2h	2h	2h	2h
Experience length (in years)	110	110	75	75

1344

1345

1346 **Table 2**

Indices/Configs	2h31	24h31	2h301	24h301	HADiSST
Niño-34 SST	0.87	0.71	0.68	0.59	0.70
IOD	0.51	0.49	0.44	0.45	0.26
EIOD	0.50	0.47	0.45	0.42	0.23
WIOD	0.26	0.26	0.23	0.22	0.21

1347

1348

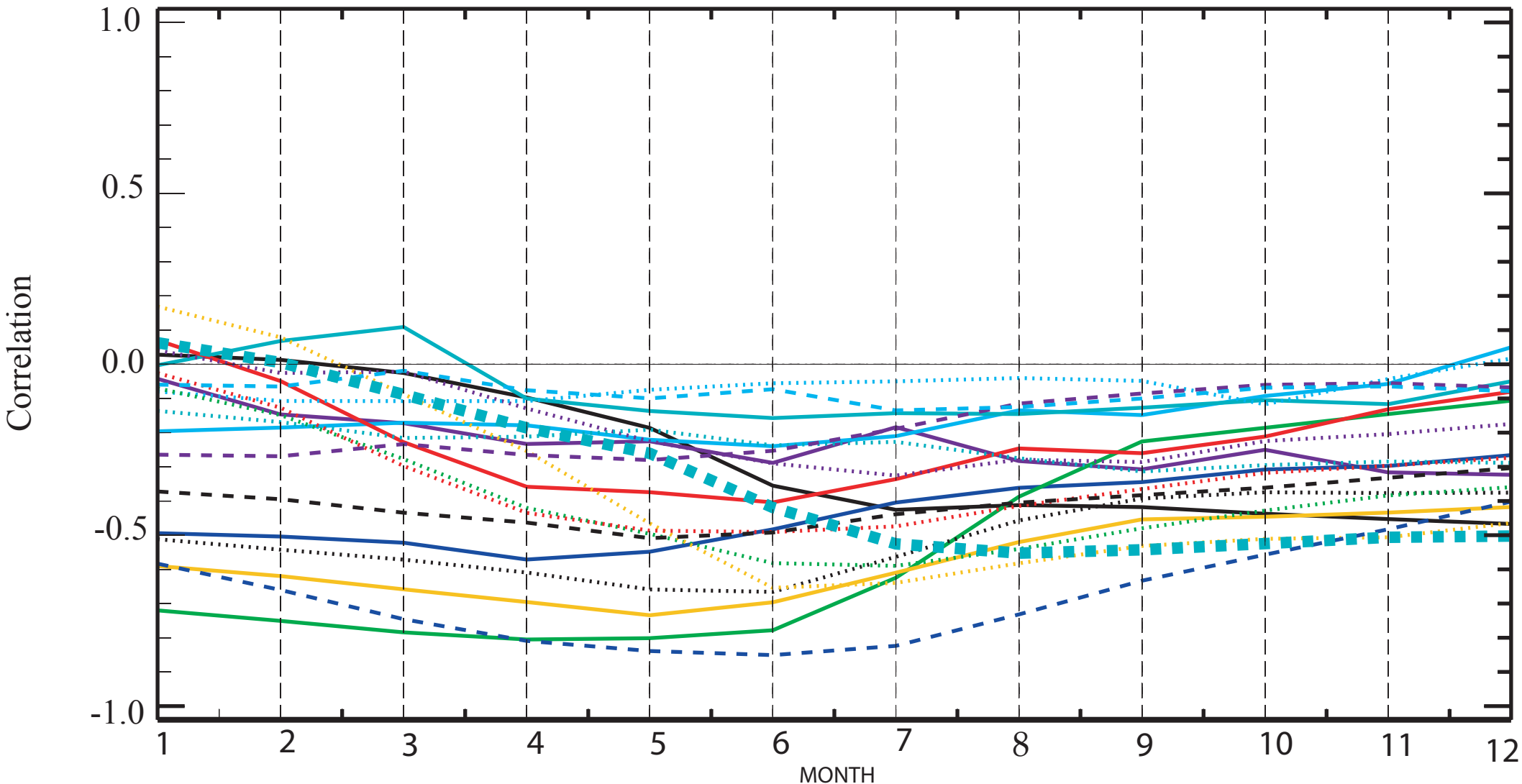
1349 **Table3**

Configuration	Land-average		Land-Ocean-average		Ocean-average	
	Mean	SD	Mean	SD	Mean	SD
CMAP	4.73	0.45	6.94	0.54	9.69	0.91
2h31	4.58	0.43	6.65	0.59	10.52	1.03
24h31	4.21	0.38	6.07	0.39	9.18	0.73
2h301	4.12	0.35	5.99	0.32	9.13	0.57
24h301	4.15	0.38	5.98	0.49	9.05	0.78

1350

Figure 1

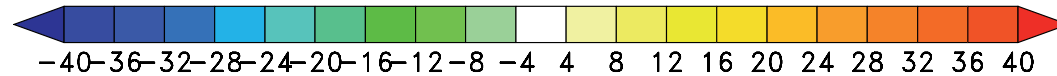
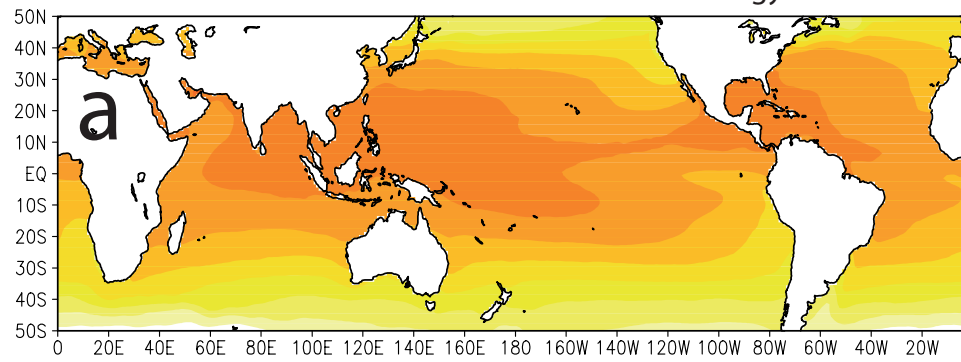
Lead-lag correlations - Monthly Nino-3.4 SST with ISM rainfall (detrended data)
20C3M Simulations



- | | | | | | |
|---|-----------------|-------|------------------|-------|--------------|
| — | GFDL-CM2.0 | | GFDL-CM2.1 | - - - | CSIRO-Mk3.0 |
| — | CGCM3.1(T47) | | CGCM3.1(T63) | - - - | INM-CM3.0 |
| — | UKMO-HadCM3 | | GISS-ER | - - - | FGOALS-g1.0 |
| — | GISS-EH | | MIROC3.2(hires) | - - - | GISS-AOM |
| — | MIROC3.2(hires) | | MIROC3.2(medres) | ■ ■ ■ | Observations |
| — | CNRM-CM3 | | IPSL-CM4 | | |
| — | ECHAM5/MPI-OM | | MRI-CGCM2.3.2 | | |
| — | PCM | | CCSM3 | | |

Figure 2

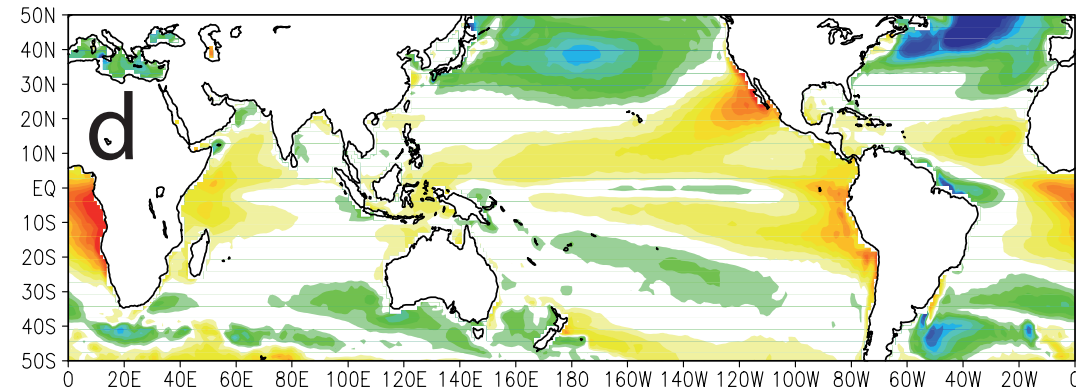
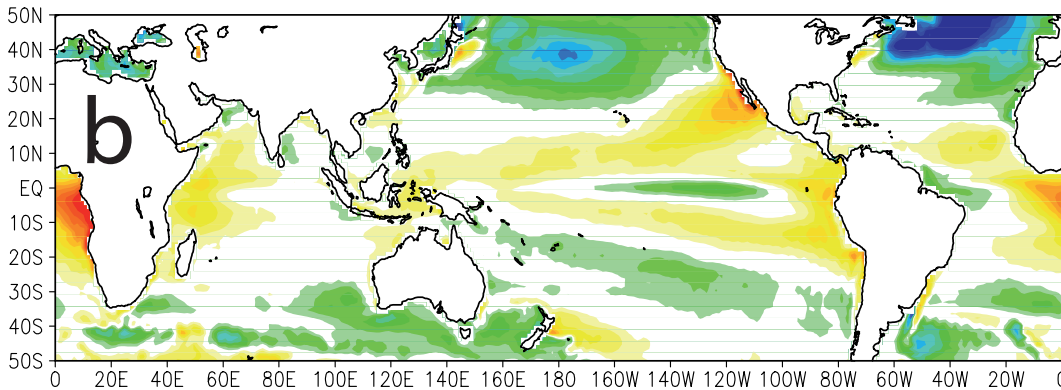
HadISST - Boreal summer climatology



2h31 - HadISST

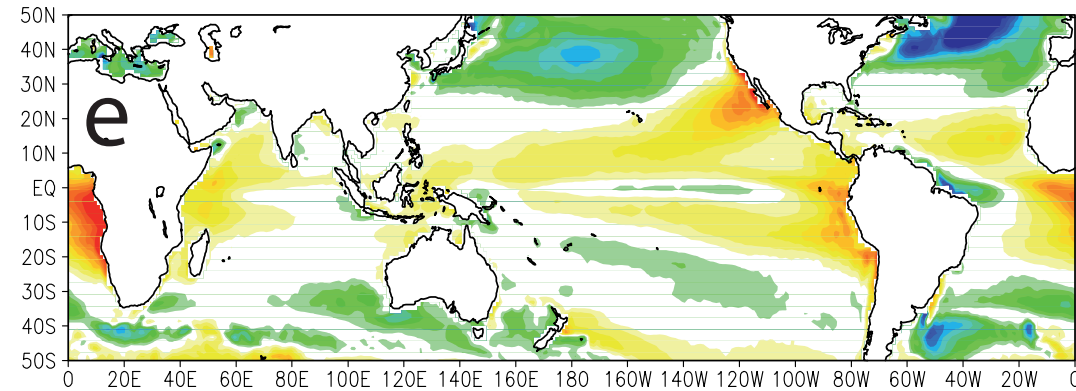
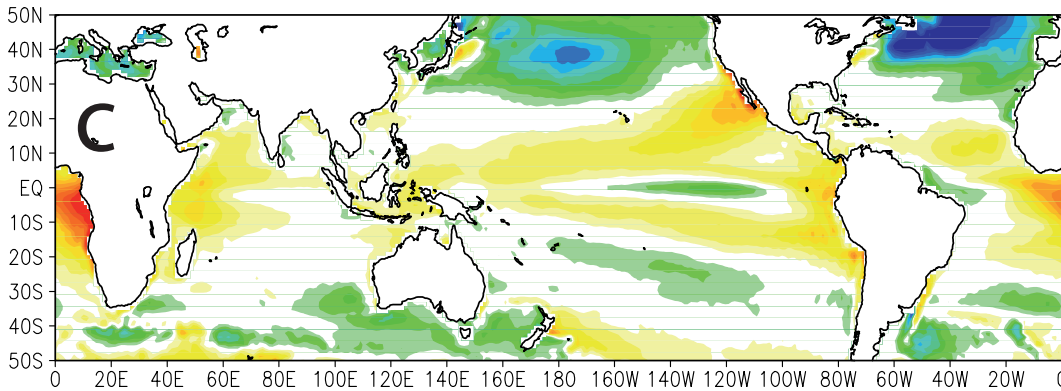
SST (°C)

2h301 - HadISST



24h31 - HadISST

24h301 - HadISST



SST bias (°C)

Figure 3

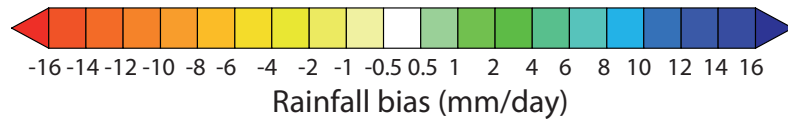
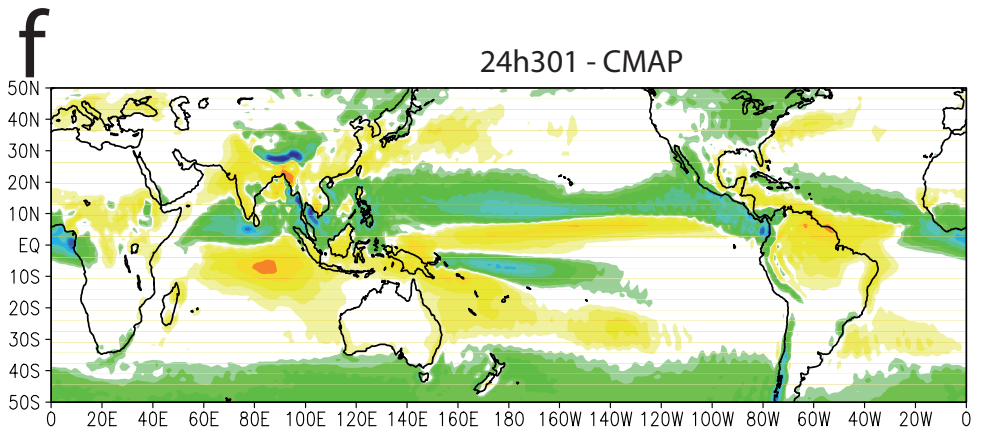
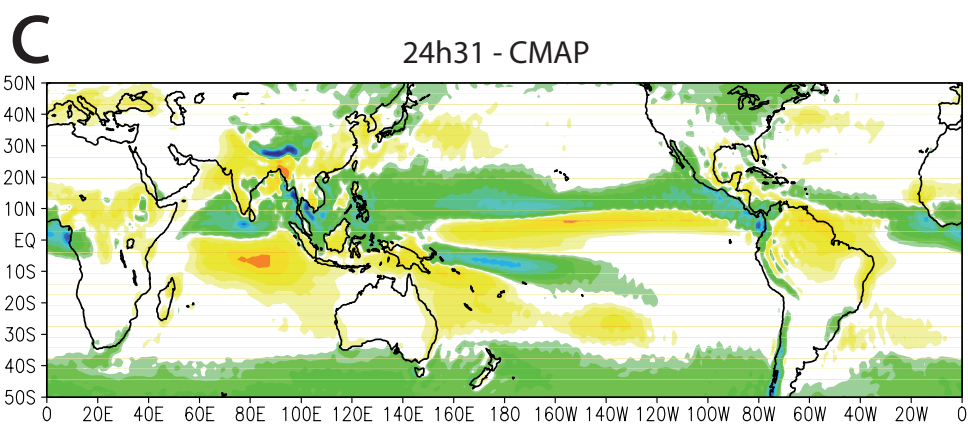
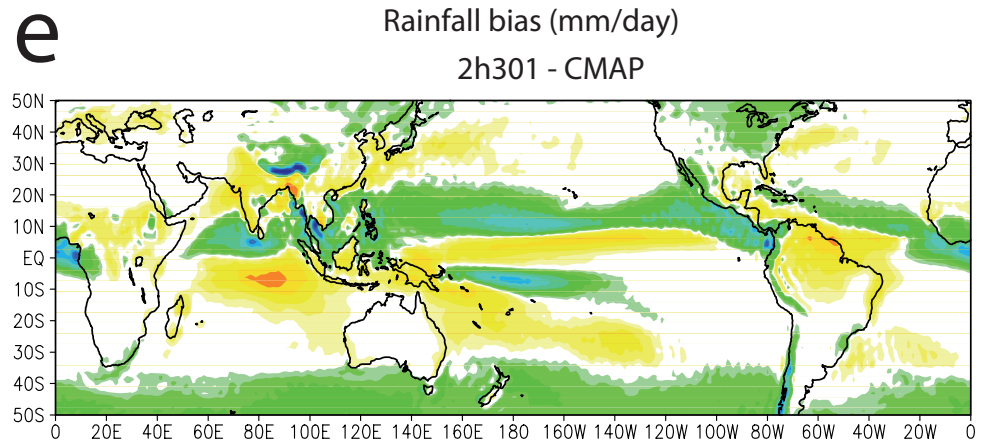
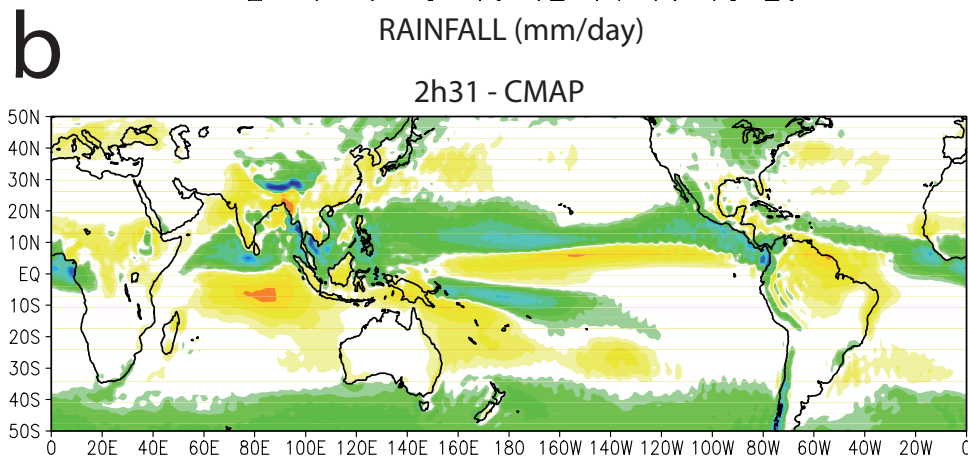
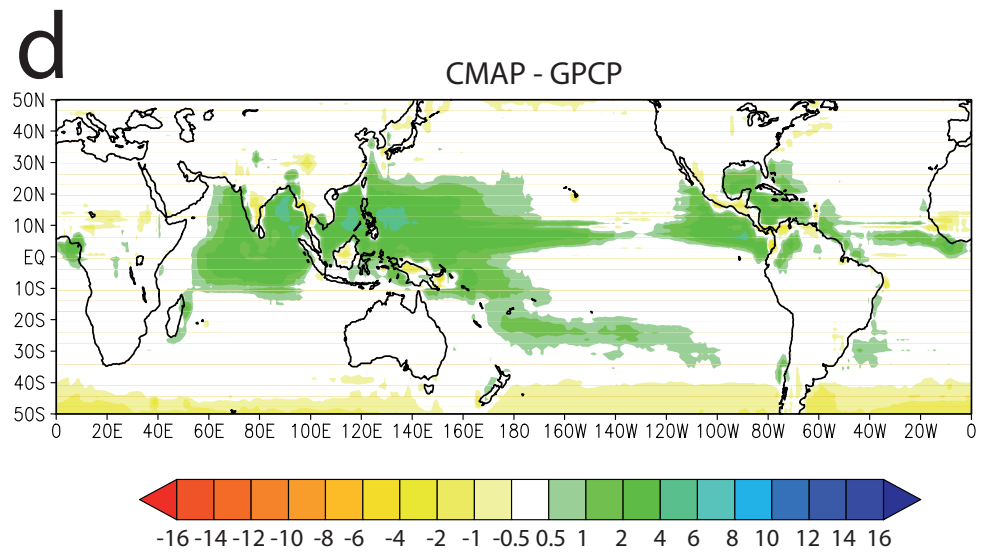
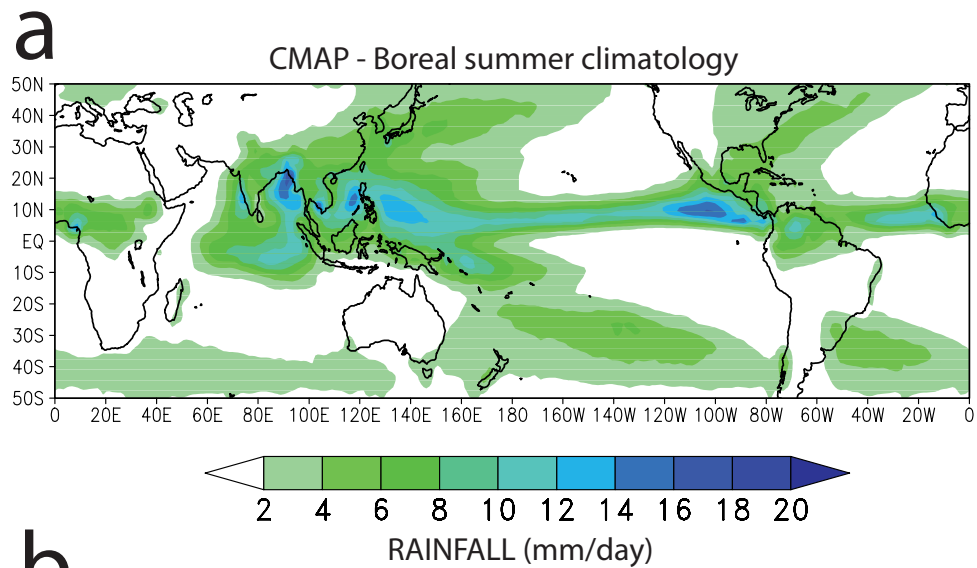
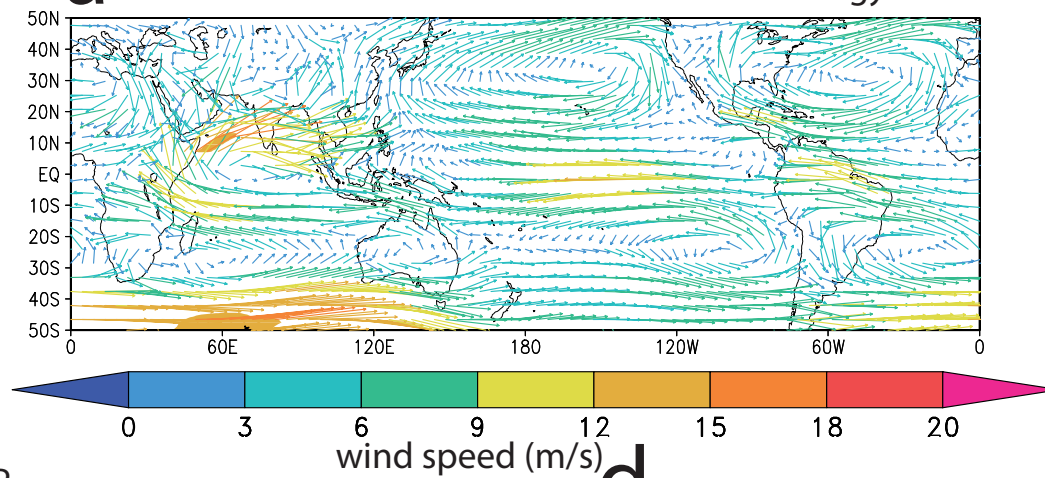
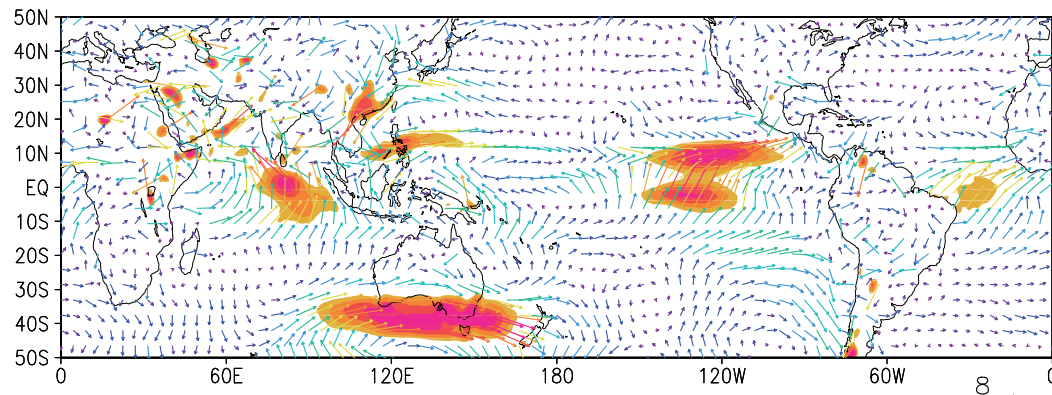


Figure 4

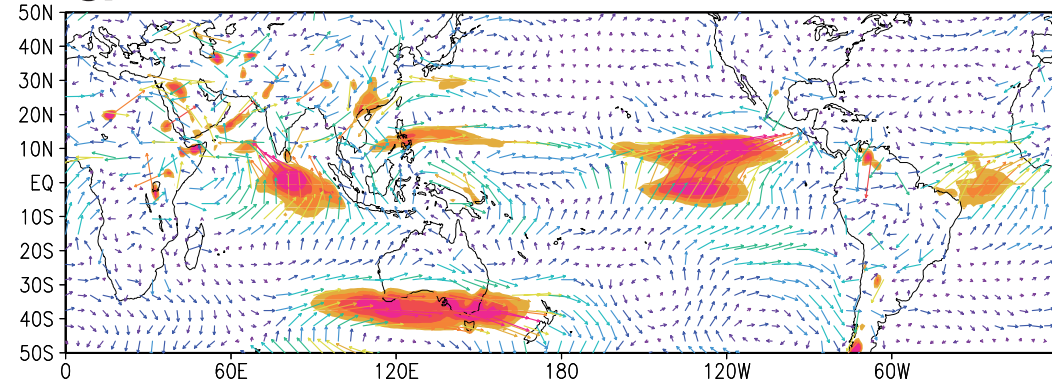
a 850 hPa NCEP wind - Boreal summer climatology



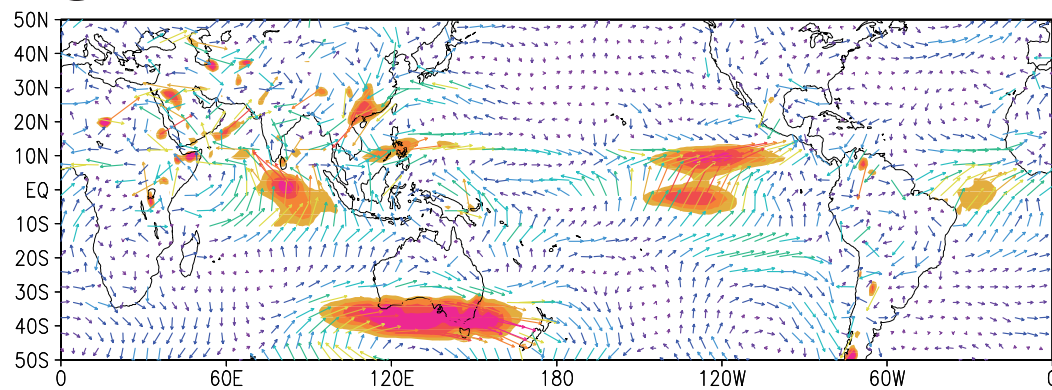
b 2h31 - NCEP



d 2h301 - NCEP



c 24h31 - NCEP



e 24h301 - NCEP

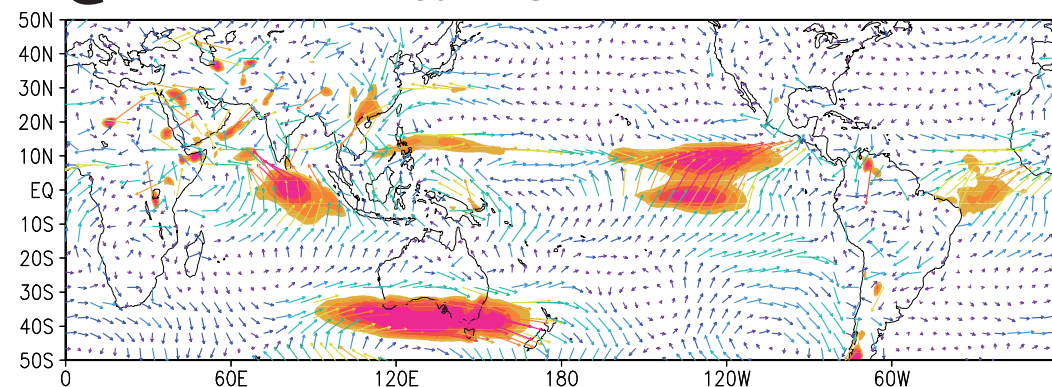


Figure 5

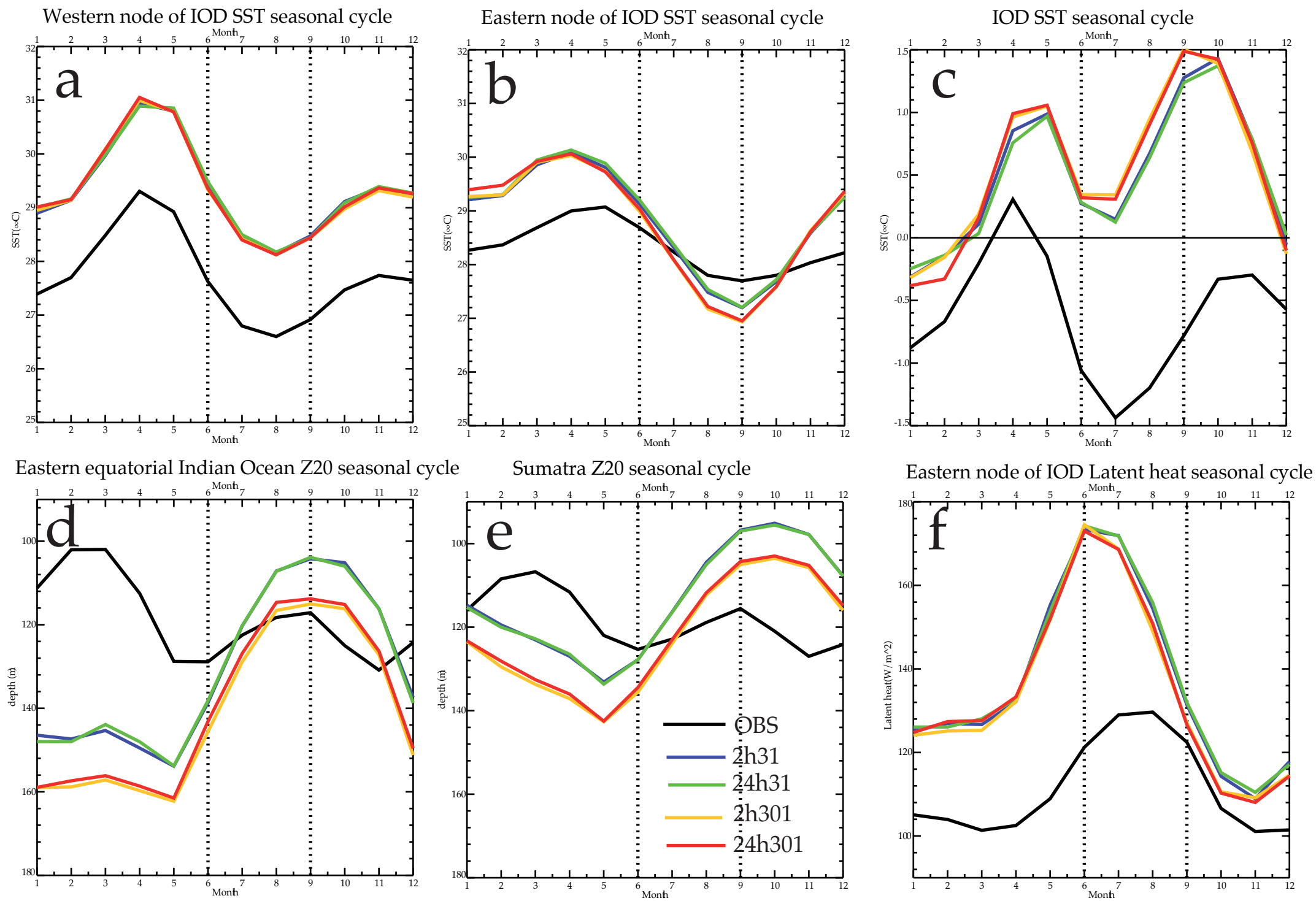


Figure 6

Seasonal cycle of rainfall (mm/day) land averaged over 65°-95°E, 8°-35°N

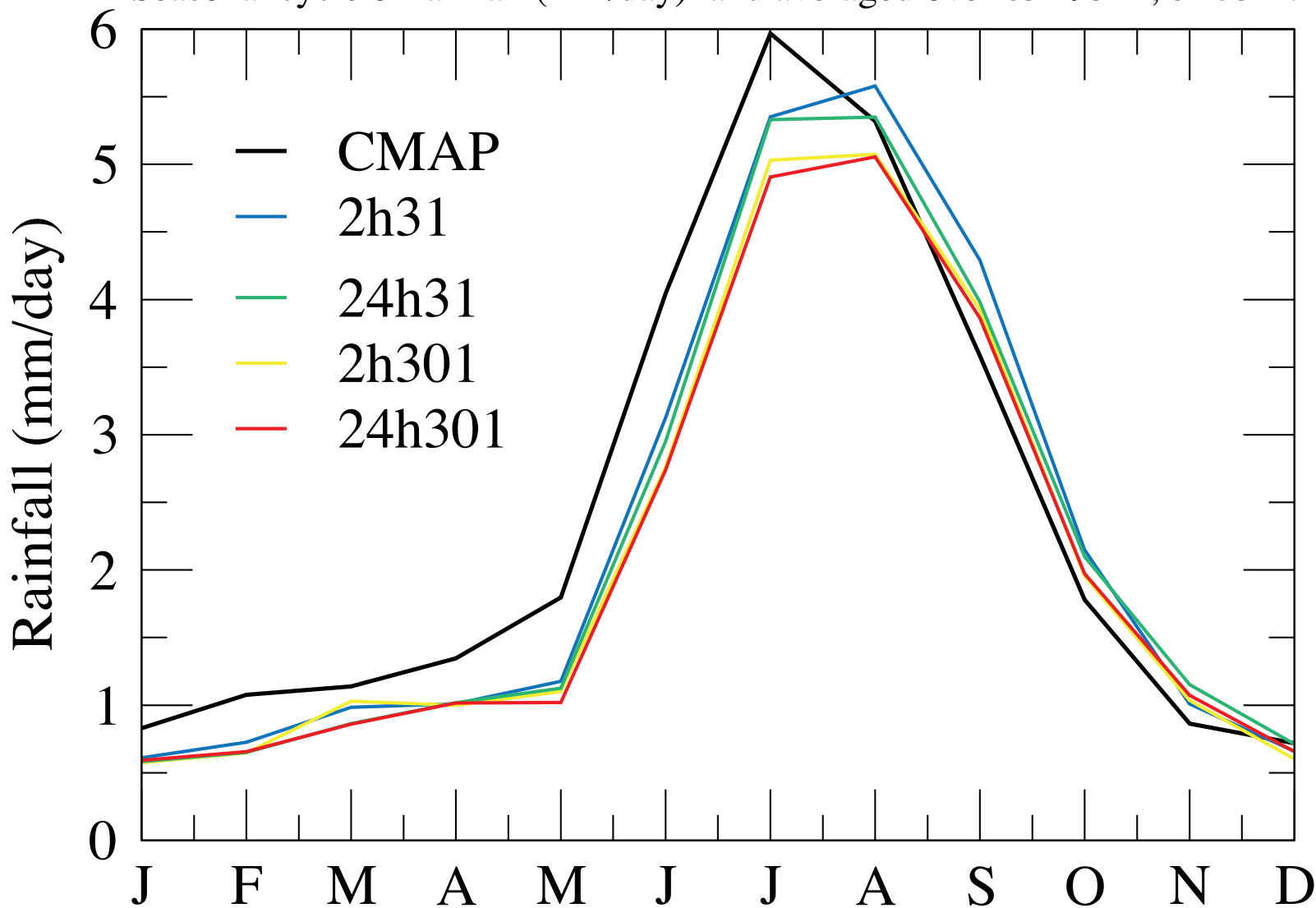
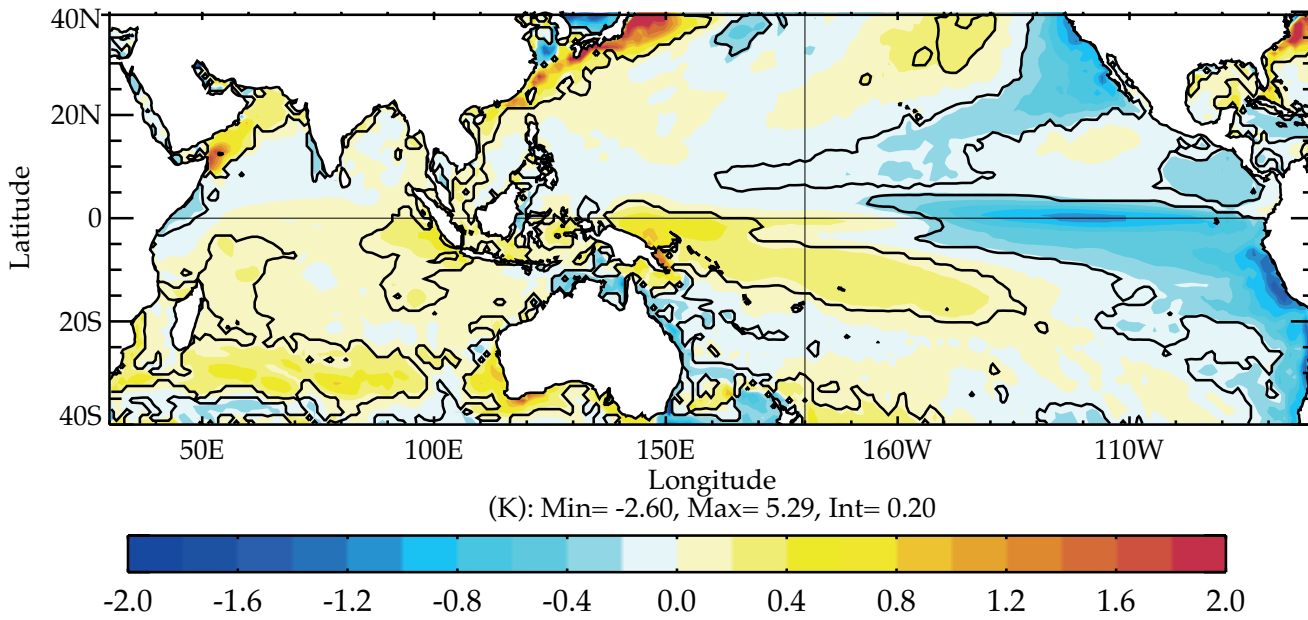


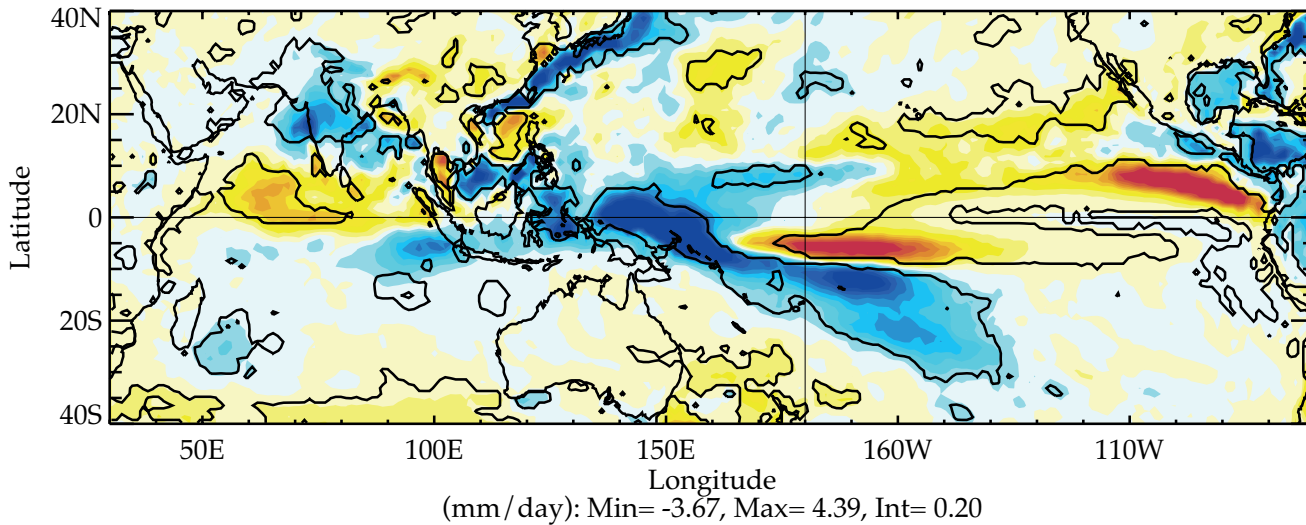
Figure 7 F31-F301 differences - June-September

a)



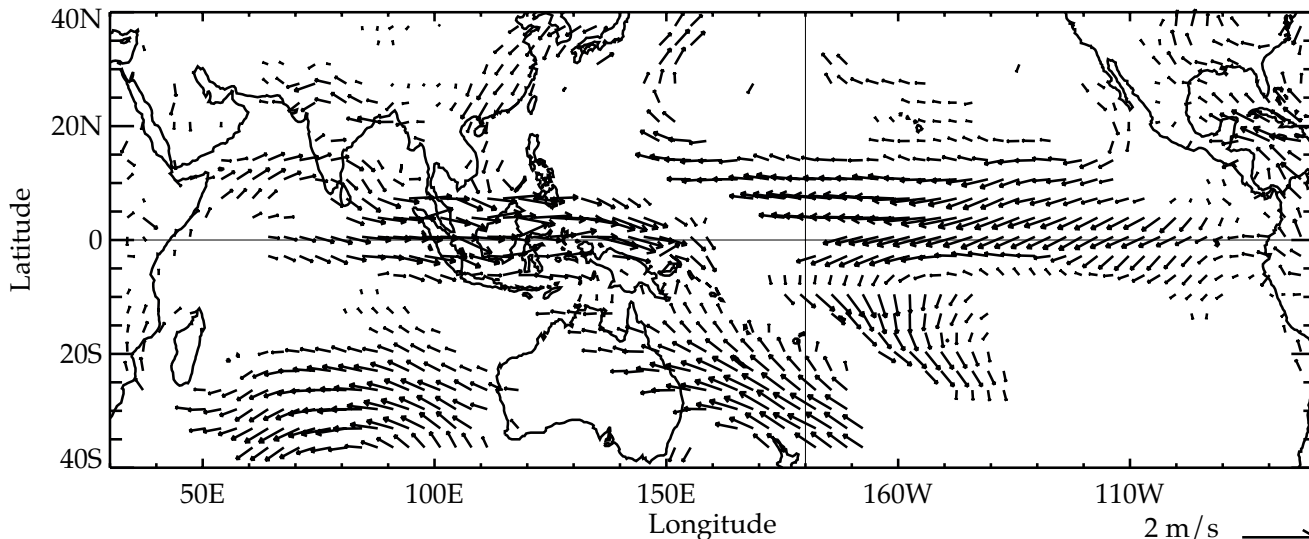
b)

SST (K)



c)

Rainfall (mm/day)



850 hPa Wind (m/s)

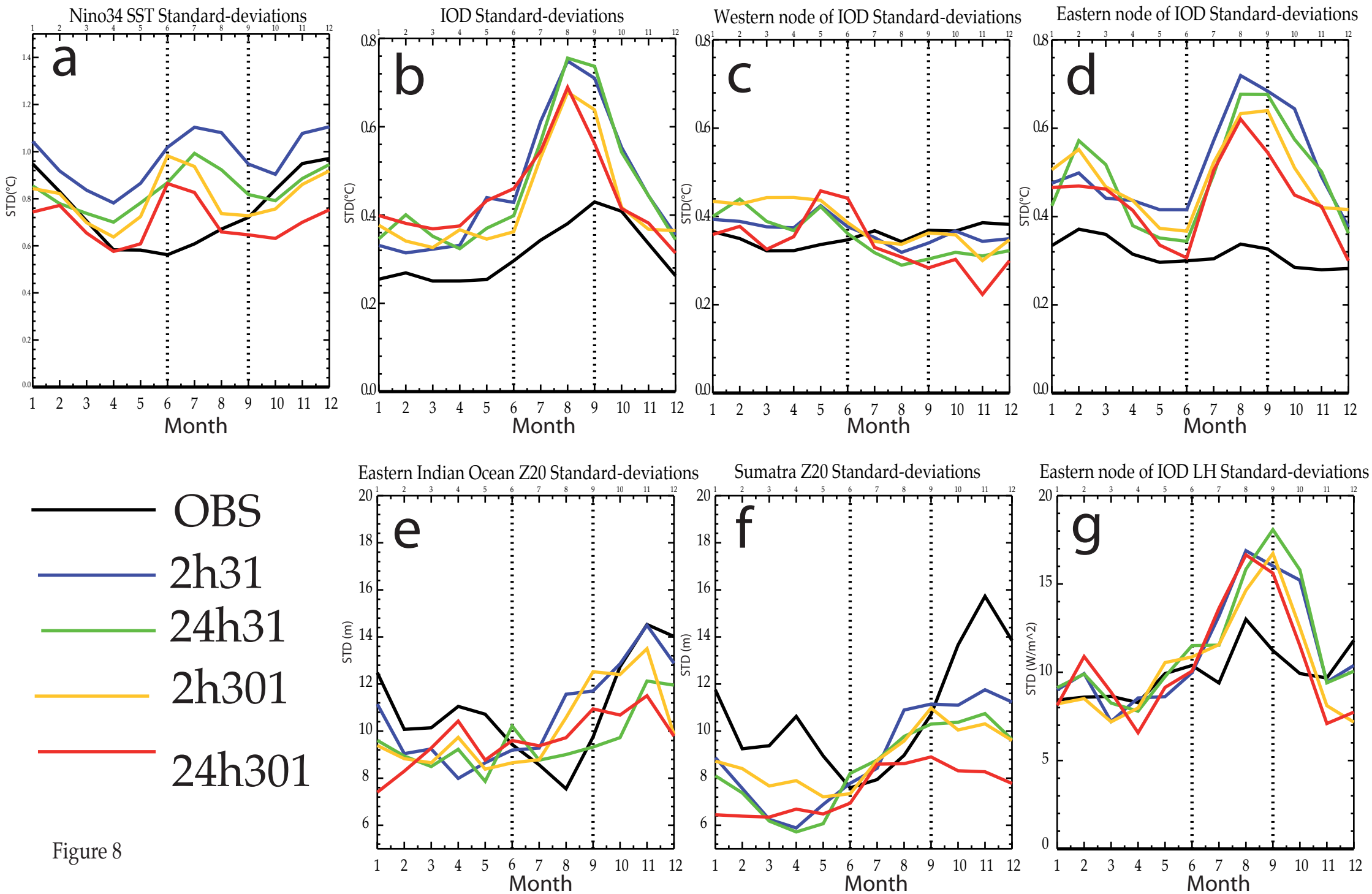


Figure 9

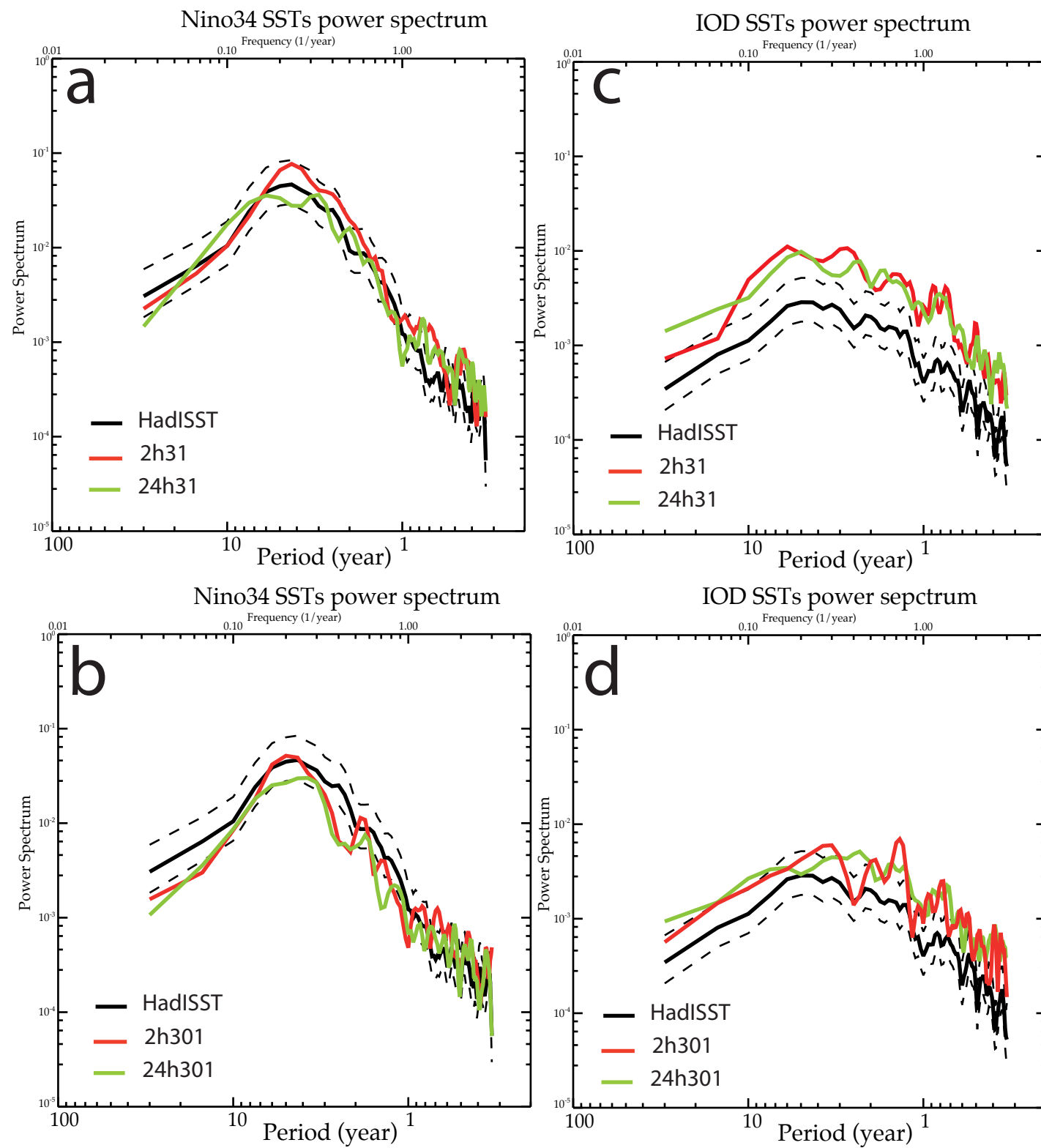


Figure 11

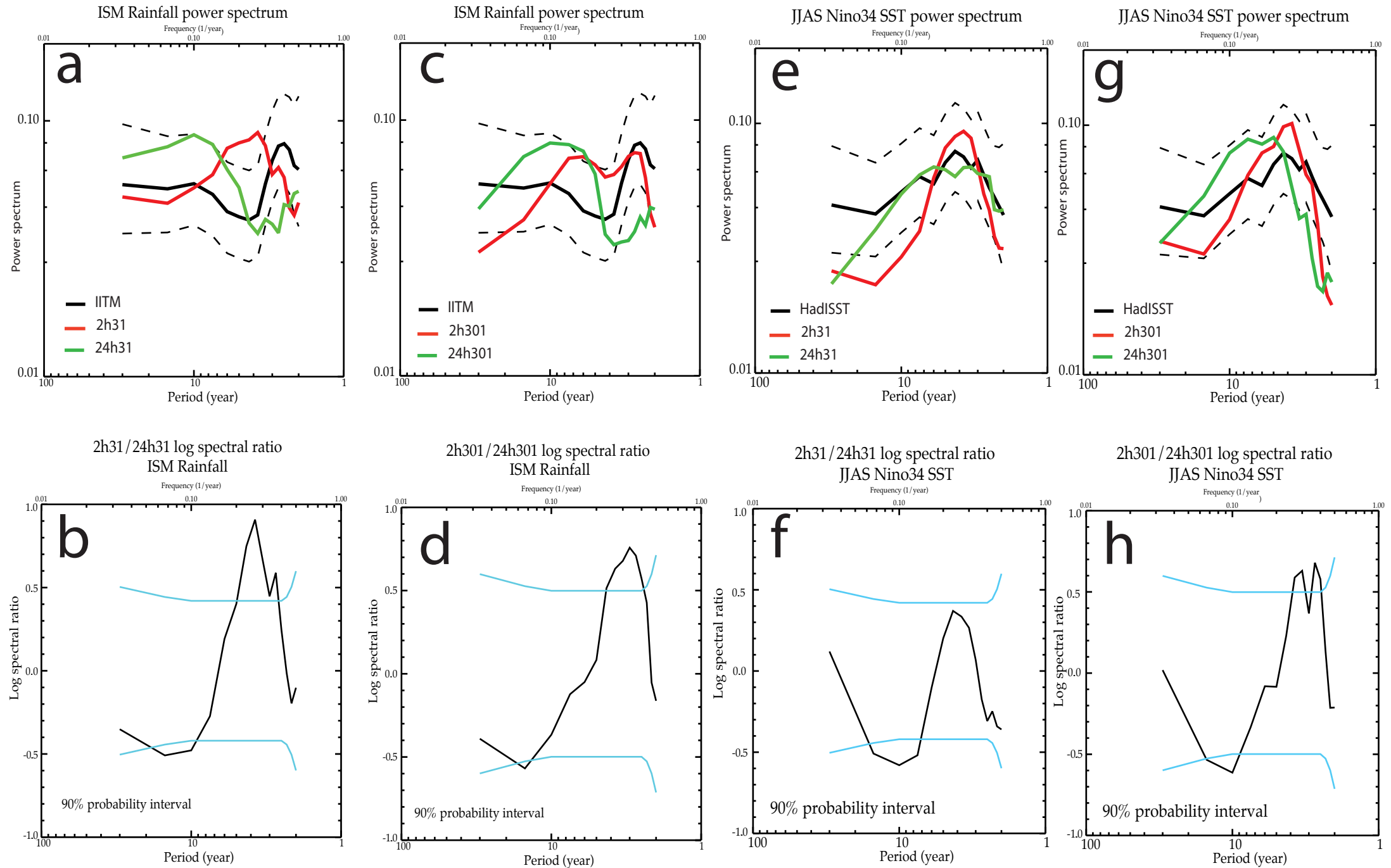
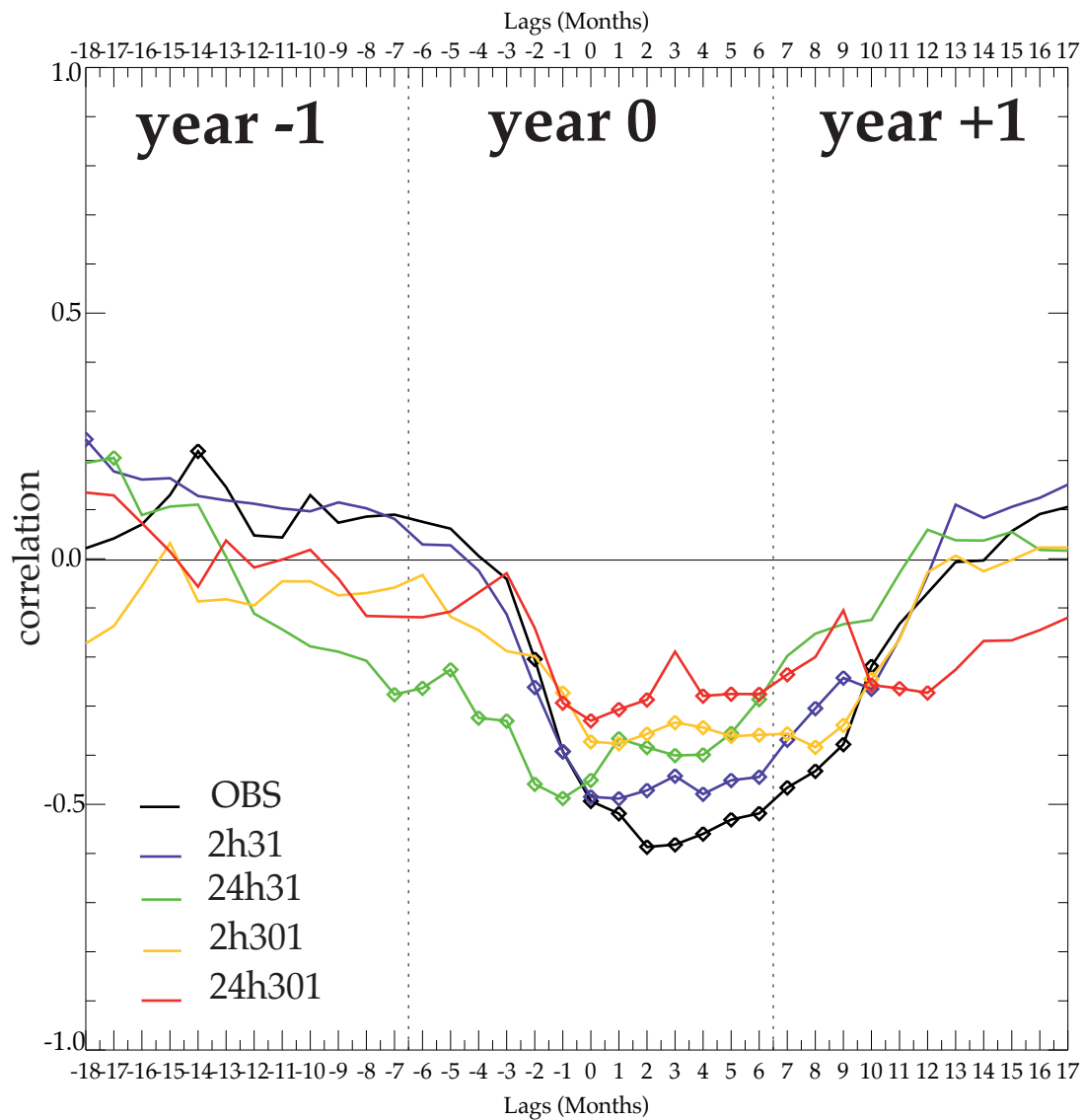


Figure 12

a

Lead-lag correlations for Monthly Nino34 SST index vs ISMR



b

Lead-lag correlations for Monthly IOD index vs ISMR

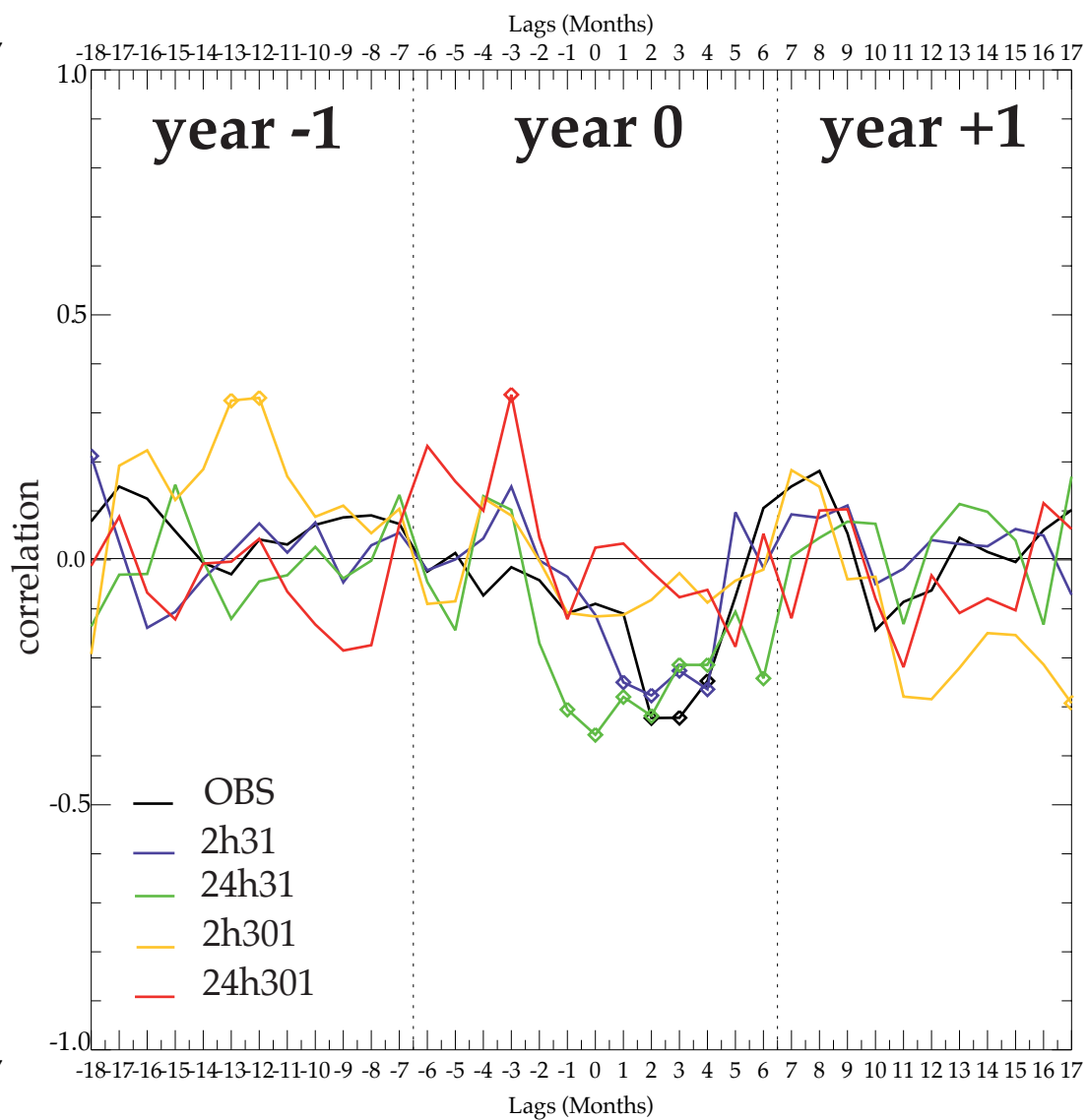
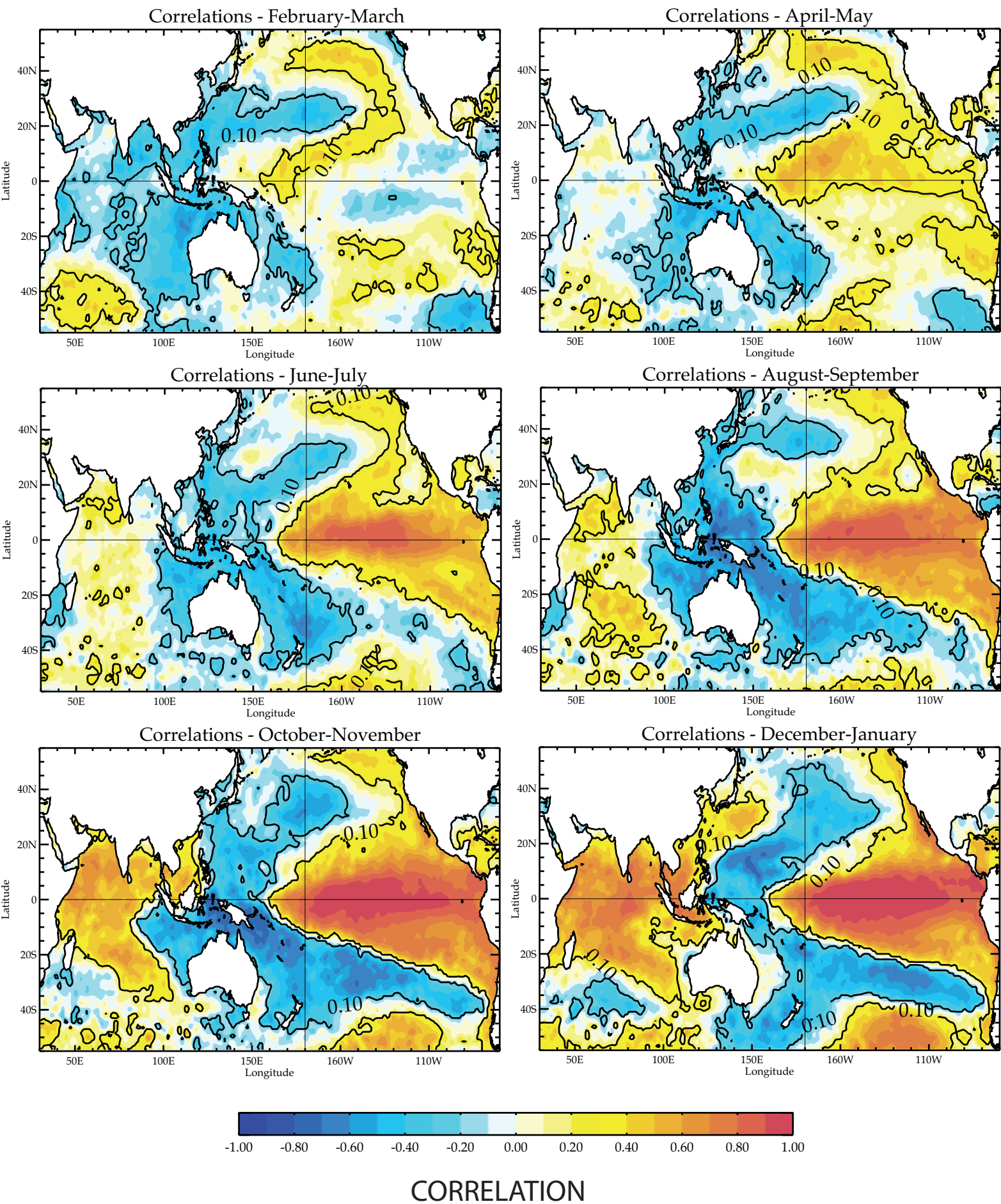


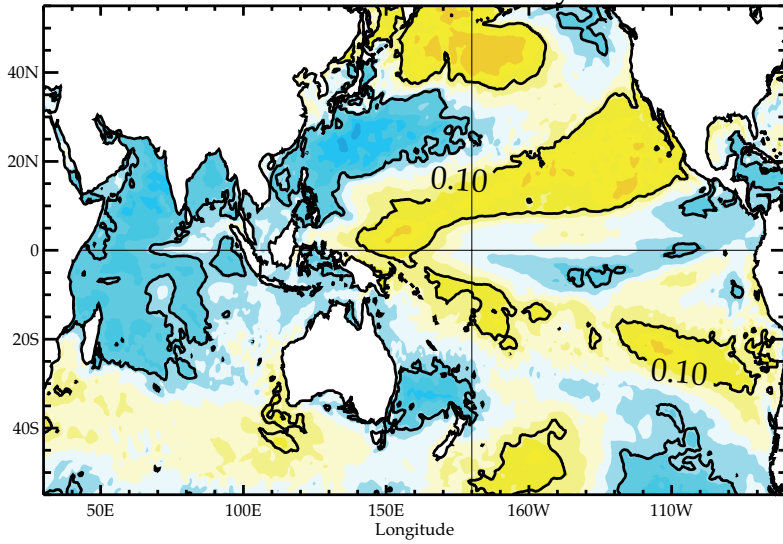
Figure 13

Correlations Nino34 SST (12-1) Indo-Pacific SSTs - HadISST1 1950-2005 - Year 0

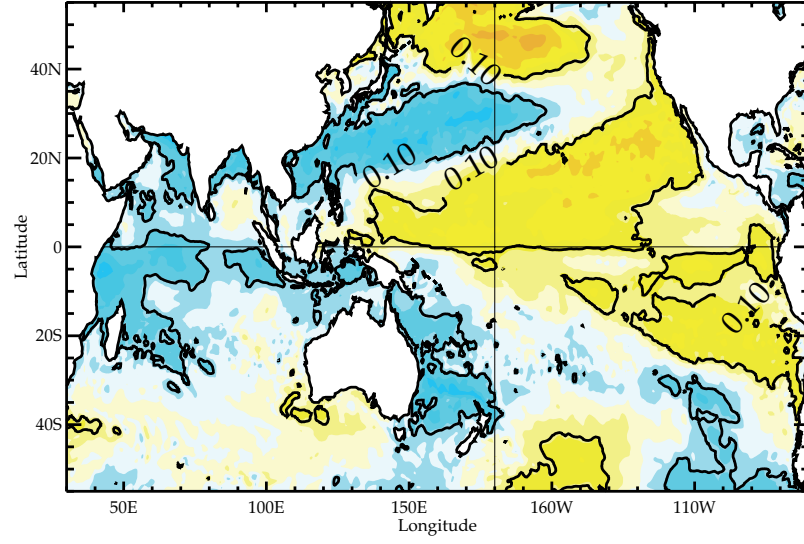


Correlations Nino34 SST (12-1) Indo-Pacific SSTs - SINTEX 2h31 - Year 0

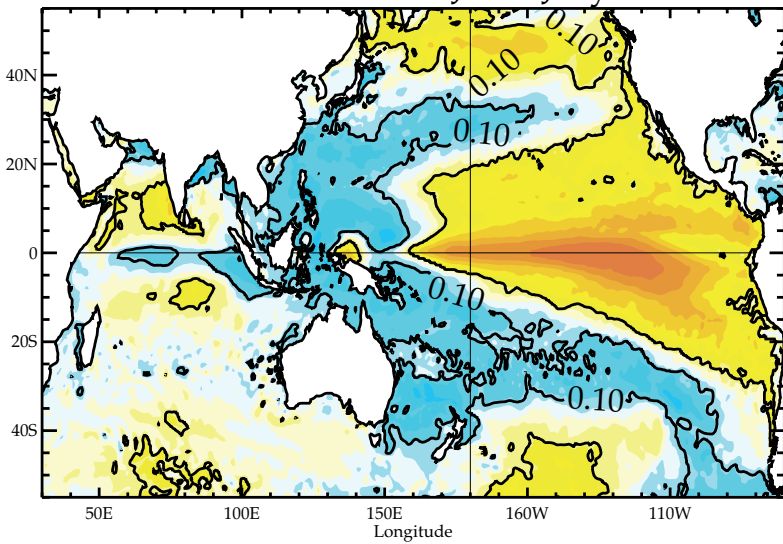
Correlations - February-March



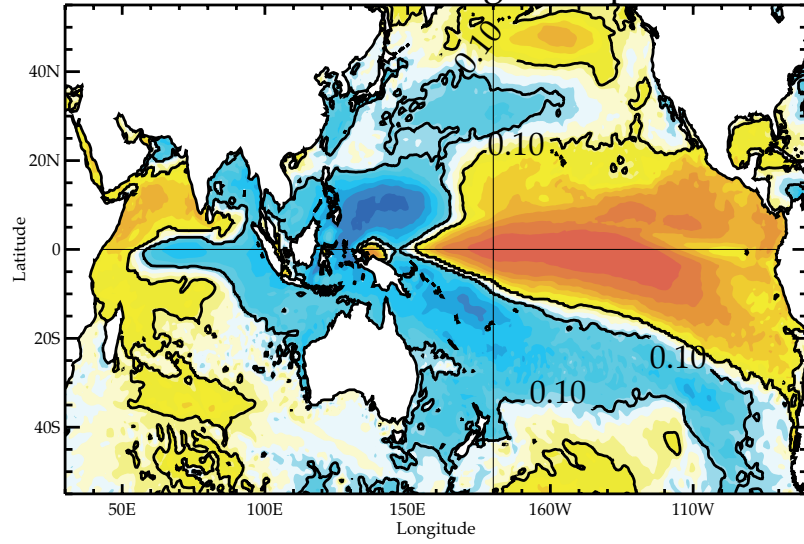
Correlations - April-May



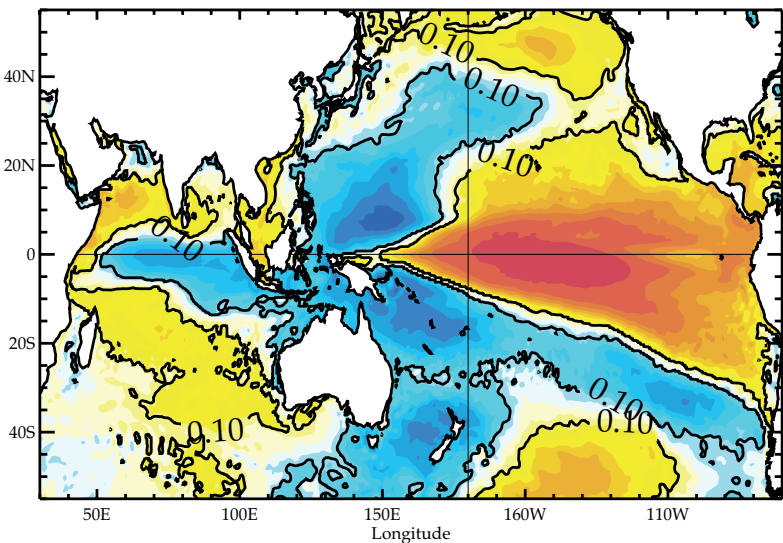
Correlations - June-July



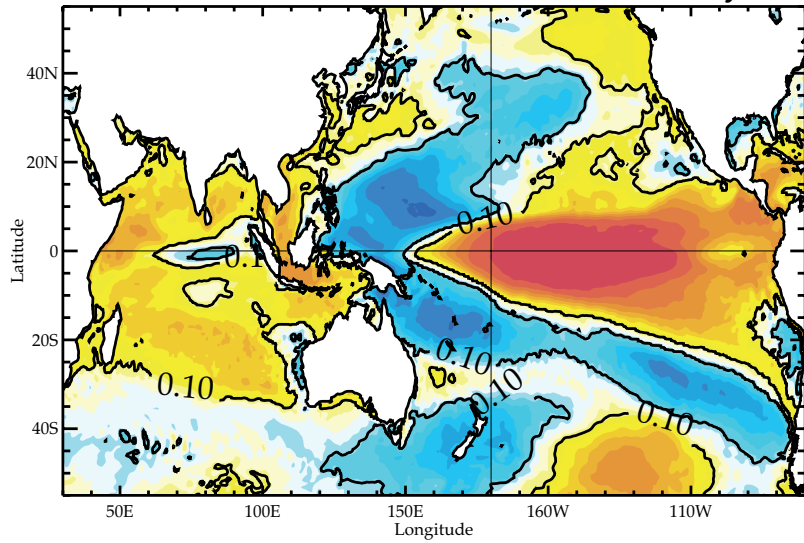
Correlations - August-September



Correlations - October-November



Correlations - December-January

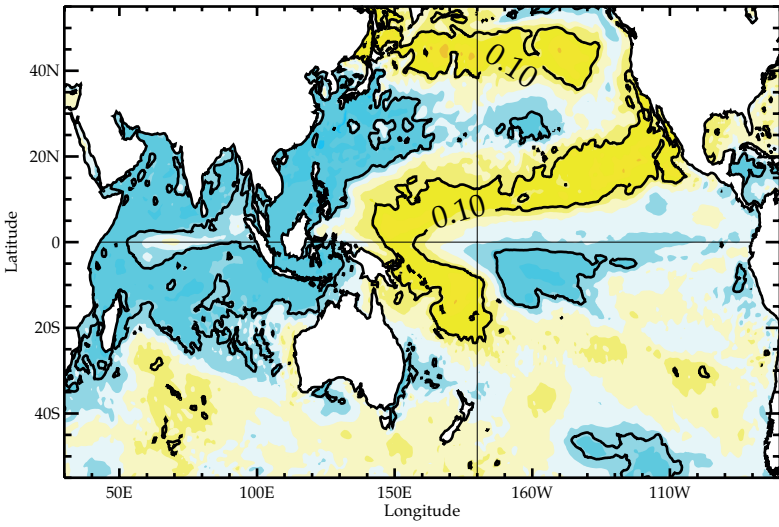


CORRELATION

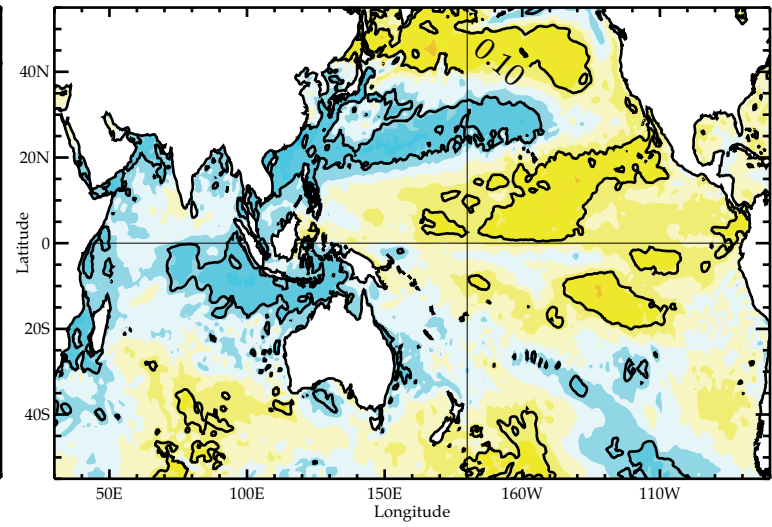
Figure 14

Figure 15

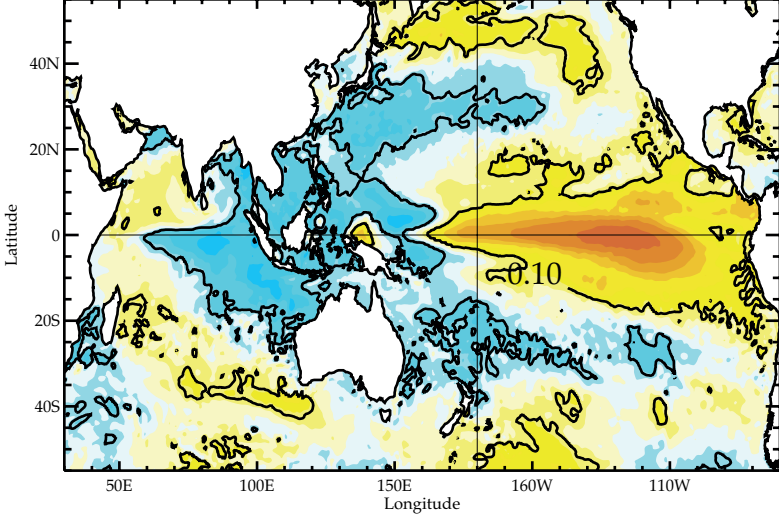
Correlations Nino34 SST (12-1) Indo-Pacific SSTs - SINTEX 24h31 - Year 0
Correlations - February-March



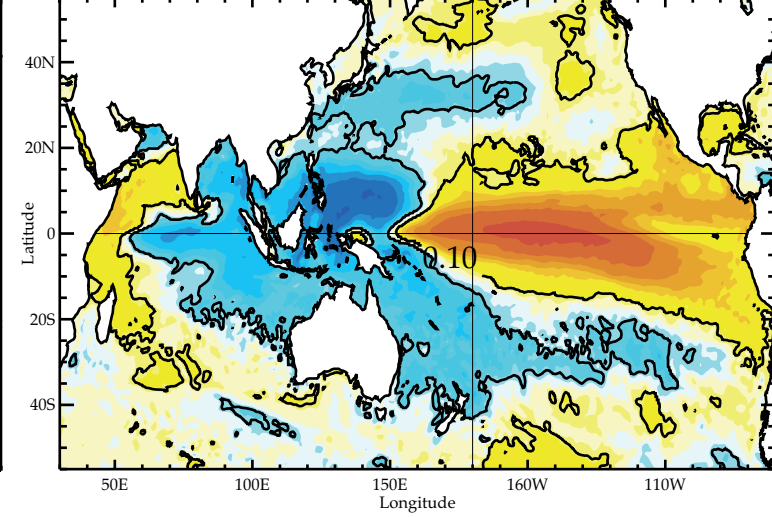
Correlations - April-May



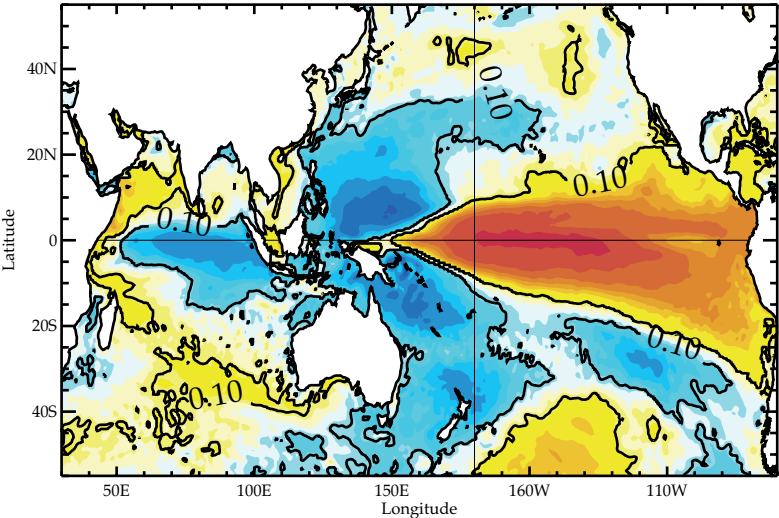
Correlations - June-July



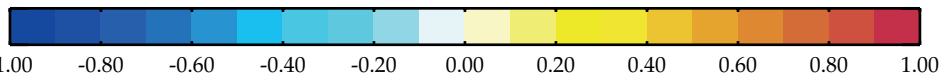
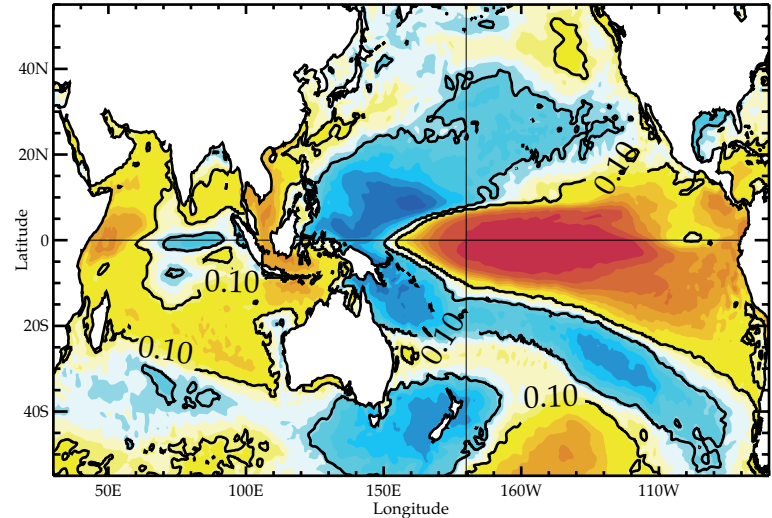
Correlations - August-September



Correlations - October-November



Correlations - December-January



CORRELATION